Long-Term Atmospheric Emissions for the Coal Oil Point Natural Marine Hydrocarbon Seep Field, Offshore California

Ira Leifer[1], Christopher Melton[1], Donald R. Blake[2]

[1]Bubbleology Research International, Solvang, CA 93463, United States

[2]University of California, Irvine, Department of Chemistry, Irvine, CA 92697, United States

Correspondence to: Ira Leifer (Ira.Leifer@bubbleology.com)

Abstract. In this study, we present a novel approach for assessing nearshore seepage atmospheric emissions through modeling of air quality station data, specifically, a Gaussian plume inversion model. Three decades of air quality station meteorology and total hydrocarbon concentration, *THC*, data were analysed to study emissions from the Coal Oil Point marine seep field offshore California. *THC* in the seep field directions was significantly elevated and Gaussian with respect to wind direction, θ. An inversion model of the seep field, θ-resolved anomaly, $THC'(\theta)$, derived atmospheric emissions. The model inversion is for the far field, which was satisfied by gridding the sonar seepage and treating each grid cell as a separate Gaussian plume. This assumption was validated by offshore *in situ* offshore data that showed major seep area plumes were Gaussian. Of plume Total Carbon, *TC*, (TC=*THC*+carbon dioxide, CO_2,+carbon monoxide) 18% was CO_2 and 82% was *THC*; methane. 85% of *THC* was CH_4. These compositions were similar to the seabed composition, demonstrating efficient vertical plume transport of dissolved seep gases. Air samples also measured atmospheric alkane plume composition. The inversion model used observed winds and derived the three-decade-average (1990-2021) field-wide atmospheric emissions of 83,400±12,000 m^3 *THC* d^{-1} (27 Gg *THC* yr^{-1} based on 19.6 g $mole^{-1}$ for *THC*).. Based on a 50:50 air to seawater partitioning, this implies seabed emissions of 167,000 m^3 *THC* d^{-1}. Based on atmospheric plume composition, C_1-C_6 alkane emissions were 19, 1.3, 2.5, 2.2, 1.1, and 0.15 Gg yr^{-1}, respectively. If CH_4 emissions were dispersed over the ~6.3 km^2 of 25x25 m^2 bins with sonar values above noise, we find 5.7 µM m^{-2} s^{-1}. The approach can be extended to derive emissions from other dispersed sources such as landfills, industrial sites, or terrestrial seepage if source locations are constrained spatially.

Deleted: ay

Deleted: y

1 Introduction

1.1 Seepage and methane

On decadal timescales, the important greenhouse gas, methane, CH_4, affects atmospheric radiative balance far more strongly than carbon dioxide, CO_2 (IPCC, 2007, Fig. 2.21), yet CH_4 has large uncertainties for many sources (IPCC, 2013) and is very sensitive to hydroxyl (OH) concentration, the primary CH_4 loss mechanism (Y. Zhao et al., 2020). Since pre-industrial times, CH_4 emissions have risen by a factor of ~2.5, and after stabilizing in the 1990s and early 2000s, resumed rapid growth since 2007 (Nisbet et al., 2019). The significantly shorter lifetime of CH_4 than CO_2 argues for CH_4 regulatory priority as emission reductions (and changes to the radiative balance) manifest more quickly as atmospheric concentrations decrease (Shindell, Faluvegi, Bell, & Schmidt, 2005). Further impetus for a CH_4 focus

is a recent estimate that 40% CH_4 emissions reductions are feasible at no net cost for the oil and gas, O&G, industry (IEA, 2020), a major anthropogenic CH_4 source (IPCC, 2014). This is particularly salient given a recent estimate that half of recent CH_4 increases are from the O&G industry (Jackson et al., 2020).

For 2008-2017, global CH_4 top-down emissions estimates are 576 Tg yr^{-1}; 1 Tg=10^{12} g, range 550-594 Tg yr^{-1}, whereas bottom-up approaches find 737 Tg yr^{-1}, range 594-881 Tg yr^{-1} (Saunois et al., 2020). A significant fraction of this discrepancy arises from uncertainty in OH concentration trends and spatial variability (Y. Zhao et al., 2020). Anthropogenic sources for 2008-2017 were estimated at 336-376 Tg CH_4 yr^{-1} based on bottom-up estimates. Natural sources include wildfires, wetlands, hydrates, and geological seepage. Bottom-up estimates for natural sources are higher than top-down estimates including for geological sources (Saunois et al., 2020). Geological sources (including seepage) are estimated at 63-80 Tg CH_4 yr^{-1} of which marine seepage is estimated to contribute 20-30 Tg CH_4 yr^{-1} (Etiope, Ciotoli, Schwietzke, & Schoell, 2019) or 5-10 Tg CH_4 yr^{-1} (Saunois et al., 2020). For comparison, marine non-geological CH_4 emissions are estimated at 4-10 Tg yr^{-1}. The broad range of this estimate arises from the uncertainty in the fraction of seabed emissions that reaches the atmosphere and the uncertainty in overall seabed emissions. Further complexity in assessing geological seepage CH_4 emissions arise because both seepage and O&G emissions source from the same geological reservoirs (Leifer, 2019) and thus are isotopically similar (Schwietzke et al., 2016).

Seepage is process by which petroleum hydrocarbon gases and fluids in the lithosphere migrate to the hydrosphere and/or atmosphere from a reservoir formation which underlies a capping layer that seals the formation, allowing hydrocarbon accumulation. Thus, seepage requires a migration pathway, typically fracture and/or fault networks, through the capping rock layer(s) (Ciotoli, Procesi, Etiope, Fracassi, & Ventura, 2020) or where the capping layer has eroded away, as an outcropping of the reservoir formation (Abrams, 2005).

Marine seepage is widespread in every sea and ocean (Judd & Hovland, 2007) and occurs primarily (but not exclusively) in petroleum systems and mostly in convergent basins (Ciotoli et al., 2020). Quantitative seepage estimates (for global budgets) are limited (though growing); see Leifer (2019) review and below for more recent. Fluxes for individual marine seep vents and seep areas have been reported for the Gulf of Mexico (C. Johansen et al., 2020; Caroline Johansen, Todd, & MacDonald, 2017; Leifer & MacDonald, 2003; Römer et al., 2019; T. C. Weber et al., 2014), the Black Sea (Greinert, McGinnis, Naudts, Linke, & De Batist, 2010), the southern Baltic Sea (Heyer & Berger, 2000), various sectors of the North Sea (Borges, Champenois, Gypens, Delille, & Harlay, 2016; Leifer, 2015; Römer et al., 2017), offshore Norway (Muyakshin & Sauter, 2010; Sauter et al., 2006) offshore Svalbard in the Norwegian Arctic (Veloso-Alarcón et al., 2019), offshore Pakistan (Römer, Sahling, Pape, Bohrmann, & Spieß, 2012), the arctic Laptev Sea (Leifer, Chernykh, Shakhova, & Semiletov, 2017), the East Siberian Arctic Sea (Shakhova et al., 2013), the South China Sea (Di, Feng, Tao, & Chen, 2020), New Zealand's Hikurangi Margin (Higgs et al., 2019), the Cascadia Margin (Riedel et al., 2018), and the Coal Oil Point (COP) marine hydrocarbon seep field, hereafter COP

Deleted: among others

Deleted: emissions
Deleted: is
Deleted: based
Deleted: on

Deleted: where
Deleted: the migration of
Deleted: escape
Deleted: the

seep field, in the northern Santa Barbara Channel, offshore Southern California (Hornafius, Quigley, & Luyendyk, 1999), and for numerous individual vents in the field (Leifer, 2010).

Most seep emission estimates are snapshot values from short-term field campaigns. Seep emissions vary on timescales from tidal (Leifer & Boles, 2005; Römer, Riedel, Scherwath, Heesemann, & Spence, 2016) to seasonal (Bradley, Leifer, & Roberts, 2010) to decadal (Fischer, 1978; Leifer, 2019). Additional temporal variability arises from transient emissions – pulses lasting seconds to minutes (Greinert, 2008; Schmale et al., 2015) to decades (Leifer, 2019). This shortcoming is being addressed by benthic (seabed) observatories and cabled observatories, e.g., Wiggins, Leifer, Linke, and Hildebrand (2015); Greinert (2008), Kasaya et al. (2009); Römer et al. (2016); Scherwath et al. (2019). Still, benthic observatories are costly and thus uncommon.

Seepage contributes to oceanographic budgets and to a lesser extent, to atmospheric budgets due to water column losses with significant uncertainty in the partitioning. As a result, uncertainty in the atmospheric contribution is much larger than the (significant) uncertainty in seabed emissions. Seepage partitioning between the atmosphere and ocean - where microbial degradation occurs on timescales inversely related to concentration (Reeburgh et al., 1991), depends primarily on depth (Leifer & Patro, 2002) with little to none of deepsea seabed emissions reaching the atmosphere, e.g., Römer et al. (2019). In contrast, very shallow seepage (meter scale) largely entirely reaches the atmosphere both by direct bubble-meditated transfer and diffusive transport. For intermediate depths, the ocean/atmospheric partitioning is complex and depends on depth, bubble flux, bubble size distribution, bubble interfacial conditions, and other characteristics (Leifer & Patro, 2002). Whereas the indirect diffusive flux (proximate and distal) depends on bubble dissolution depth (Leifer & Patro, 2002), vertical turbulence transport in the winter wave-mixed layer (Rehder, Keir, Suess, & Rhein, 1999), microbial oxidation losses, and exchange through the sea-air interface.

A range of approaches have been used to estimate the sea-air flux. The most common is by measuring the atmospheric and water concentrations and applying air-sea gas exchange theory for the measured wind speeds, e.g., Schmale, Greinert, and Rehder (2005) for Black Sea seepage under weak wind speeds. Sea-air exchange is a diffusive turbulence transfer process that depends on the air-sea concentration difference and the piston velocity, k_T, which depends on gas physical properties, wind speed, u (Liss & Duce, 2005), wave development (D. Zhao, Toba, Suzuki, & Komori, 2003) including wave breaking (Liss & Merlivat, 1986), and surfactant layers at low wind speeds that suppress gas exchange (Frew et al., 2004). k_T increases rapidly and non-linearly with u and has been parameterized by piecewise linear functions (Wanninkhof, Asher, Ho, Sweeney, & McGillis, 2009) or by a cubic function (Nightingale et al., 2000). Air-sea gas exchange theory is for (relatively) homogeneous atmospheric and oceanographic fields (concentrations, winds, and wave development), and thus is inappropriate for point-source (bubble-plume) emissions and for the near-field downcurrent plume, which tend to be heterogeneous.

Another approach uses seabed bubble size measurements or an assumed bubble size distribution to initialize a numerical bubble propagation model to predict direct bubble-mediated atmospheric fluxes (Leifer et al., 2017; Römer

Deleted: which

Deleted: turbulence

Deleted: as

Deleted: as

et al., 2017; Schneider von Deimling et al., 2011). The dissolved portion that evades to the atmosphere could be addressed by a dispersive model coupled to an air-sea gas exchange model, though studies have not yet addressed this component.

An alternate approach is to derive atmospheric emissions by plume inversion. Leifer, Luyendyk, Boles, and Clark (2006) derived emissions for a blowout from Shane Seep in the COP seep field by a plume inversion. This neglected the portion that dissolves during bubble rise and drifts downcurrent, out of the bubble plume's vicinity before sea-air gas transfer into the atmosphere. Note dissolved gas evasion in the plume vicinity contributes to the inversion emissions estimate.

1.2 Study motivation

In this study, we present a novel approach for assessing nearshore seepage atmospheric emissions – air quality station data modeling, specifically using a Gaussian plume inversion model. This model requires that source locations are mapped, spatially stable, and lie within a fairly constrained distance range band. These conditions are met for the COP seep field, which is near the West Campus air quality Station (WCS). COP seep field lies in shallow coastal waters of northern Santa Barbara Channel, CA. Spatial constraint is provided by geological structures, such as faults, that constrain emission locations. The Gaussian plume model assumes a far-field source, whereas WCS is in the nearfield of the extensive COP seep field. To satisfy the far field criterion, the source was gridded and each grid cell's emissions treated as a distinct (distant) Gaussian plume. This characterization was validated in an offshore survey of several focused COP seep field seepage areas, which were well-modeled as Gaussian plumes.

Thus, this study demonstrates an approach to deriving emissions from air quality station data for an area source such as natural marine seepage. This approach could be used to derive emissions from other dispersed sources such as landfills, industrial sites, or natural terrestrial seepage where the source locations are constrained spatially.

1.3 Water column marine seabed seepage fate

Seep seabed CH_4 partitioning between the atmosphere and water column depends on seabed depth and emission character – as bubbles, bubble plumes (Leifer & Patro, 2002), or dissolved CH_4. Dissolved CH_4 migration through the sediment is oxidized largely by near seabed microbes (Reeburgh, 2007), termed the microbial filter, negating its contribution, leaving only bubble-mediated flow.

As seep bubbles rise, they dissolve, losing gas to the surrounding water at a rate that decreases with time. Smaller and more soluble gases dissolve faster than larger and less soluble gases, i.e., fractionation (Leifer & Patro, 2002). Additionally, larger bubbles transport their contents upwards more efficiently than smaller bubbles (Leifer et al., 2006). Sufficiently large bubbles reach the sea surface with a significant fraction of their seabed CH_4 from depths of

Deleted: the
Deleted: is in the far field
Deleted: for
Deleted: can
Deleted: be
Deleted: ;
Deleted: smaller

even hundreds of meters (Solomon, Kastner, MacDonald, & Leifer, 2009). There are synergies, too with higher plume fluxes driving a stronger upwelling flow that transports plume fluids with dissolved gases upwards towards the surface where air-sea gas exchange drives evasion (Leifer, Jeuthe, Gjøsund, & Johansen, 2009). Another synergy arises from elevated dissolved plume CH_4 concentration (Leifer, 2010; Leifer et al., 2006), which slows dissolution. Also, bubbles are oil-coated, which slows dissolution.

Moreover, gases in bubbles that dissolve in the wave-mixed layer (or reach it by the upwelling flow) then diffuse to the air-sea interface due to wave and wind turbulence. Note, microbial degradation removes a portion of the dissolved CH_4, which therefore never reaches the air-sea interface. Thus, there are two timescales that govern the fraction that evades – the microbial degradation timescale, which increases as concentrations decrease, and the diffusion timescale, which decreases with increasing wind speed. As a result, there is a dissolved plume that drifts downcurrent, with evasion from this drifting plume creating a linear-source atmospheric plume. Note, dissolved plume concentrations slowly decrease with time (downcurrent distance) from sea-air gas exchange losses, microbial oxidation, and dispersion, leading to a decreased atmospheric plume.

Deleted: decreases
Deleted: increase
Deleted: from
Deleted: which
Deleted: creates
Deleted: with
Deleted: decreasing

1.4 Atmospheric Gaussian plumes

Strong focused atmospheric plumes are created from seep plume bubbles bursting at the sea surface and from dissolved gas evasion within the bubble surfacing footprint. This evasion is enhanced by water-side turbulence from rising and bursting bubbles (Leifer et al., 2015). Atmospheric plume evolution is described by the Gaussian plume model (Hanna, Briggs, & Hosker Jr., 1982), which relates downwind concentrations to wind transport and turbulence dispersion and is the basis of the inversion calculation (see Supp. Sec. S1 for details).

Deleted: the

1.5 Setting

1.5.1 The Coal Oil Point seep field

The COP seep field (Fig. 1) is one of the largest seep fields in the world, with estimated 1995-1996 seabed total hydrocarbon, *THC*, emissions, E_B, of $1.5x10^5 \pm 2x10^4$ m^3 d^{-1} (Hornafius et al., 1999). Hereafter emissions and concentrations are for *THC* unless noted. Clark, Washburn, Hornafius, and Luyendyk (2000) estimated that half the COP seep field E_B reach the atmosphere in the near field. This is due to shallowness, bubble oiliness, high plume bubble densities, and turbulence mixing within the wave mixed layer.

Deleted: *THC*
Deleted: y
Deleted: total hydrocarbon,

Geological structures play a critical role in the spatial distribution of seepage (Leifer, Kamerling, Luyendyk, & Wilson, 2010), which lies along several trends in waters from a few meters to ~85 m deep. These trends follow geologic structures including anticlines, synclines, and faults in the reservoir formation, the Monterey Formation and overlying Sisquoc Formation. Faults and fractures associated with damage zones provide migration pathways with seepage scattered non-uniformly along the trends, including focused seep areas that are highly active, localized, and often are

associated with crossing faults and fractures (Leifer et al., 2010). Seepage in these areas typically surrounds a focus and decreases with distance, primarily along linear trends (Leifer, Boles, Luyendyk, & Clark, 2004). See Supp. Table S3 for informal names and locations of selected focused seep areas.

1.5.2 Coal Oil Point seep field emissions and composition

COP seep field sources from the South Ellwood oil field whose primary source rock is Monterey Formation, which is immature to marginally mature. Petroleum gases from marine organic materials have relatively higher proportion of ethane, propane, butane, etc., relative to methane as compared to petroleum gases from terrestrial organic materials. The wet gas fraction (C_2-C_5/C_1-C_5) indicates a thermogenic origin of greater than 0.05 (Abrams, 2017). Of the saturated alkanes, the alkenes (olefins) are of biological origin. Additionally, the ethane/ethene ratio and propane/propene ratios can be indicators of seep gas biogenic modification with values above 1000 indicating purely thermogenic origin (Abrams, 2017; Bernard, Brooks, & Zumberge, 2001).

In this study, we analyse WCS (located at 34° 24.897'N, 119° 52.770'W) atmospheric *THC*. Clark, Washburn, and Schwager (2010) report average seep field seabed CH_4, CO_2, and non-methane hydrocarbons (NMHC), of 76.7, 15.3, and 7.7%, respectively, with Trilogy Seep seabed compositions of 67, 21, and 7.8%, respectively. With respect to alkanes, seabed bubbles are 90.4% CH_4 and 8.6% NMHC. CO_2 rapidly escapes the bubbles and is negligible (<1%) at the sea surface. At the sea surface, CH_4 in bubbles is ~90% with NMHC making up the remaining 10%, neglecting air gases (Clark et al., 2010). Note, whereas seep *THC* is predominantly CH_4, *THC* from terrestrial directions arises from NMHC from traffic and other anthropogenic sources as well as CH_4 from pipeline leaks, terrestrial seeps, etc.

Formatted: Font: Italic

Formatted: Font: Italic

Formatted: Font: Italic

1.5.3 Northern Santa Barbara Channel climate

Diurnal and seasonal wind cycles are important to the atmospheric transport of COP seep field emissions. The Santa Barbara climate is Mediterranean with a dry season and a wet seasons when storms occur infrequently (Dorman & Winant, 2000). The semi-permanent eastern Pacific high-pressure system plays a dominant controlling role in weather in the Santa Barbara coastal plain. This high-pressure system drives light winds and strong temperature inversions that act as a lid that restricts convective mixing to lower altitudes. The coastal California boundary layer is shallow, from 0 to 800 m thick (Edinger, 1959); generally 240-300 m around Santa Barbara (Dorman & Winant, 2000). Additionally, coastal mountains provide physical barriers to transport (Lu, Turco, & Jacobson, 1997).

As a coastal environment, the land/sea breeze is important to overall wind-flow patterns with weak offshore night winds and stronger onshore afternoon winds (Dorman & Winant, 2000). In coastal Santa Barbara, warming on mountaintops and more interior arid lands relative to cooler marine temperatures drives the sea breeze. Downslope nocturnal flows warm nocturnal surface temperatures, moderating the coastal diurnal temperature cycle (Hughes, Hall, & Fovell, 2007).

Typical morning winds are calm and offshore and often accompanied by a cloud-filled marine boundary layer, 50–150 m thick (Lu et al., 1997). The marine layer usually (but not always) "burns off" mid–morning after which temperatures rise, the boundary layer thickens and winds shift clockwise from offshore to eventually prevailing westerlies aligned with the coastal mountains. Midday through late afternoon and even evening, winds strengthen, often leading to whitecapping before the boundary layer collapses and winds return to the nocturnal pattern.

Deleted: resume

2 Methods

2.1 West Campus Station data

WCS data includes wind speed, u, and direction, θ, by a vane anemometer (010C,020C, Met One, Grants Pass, OR) and *THC* concentration, C, by a Flame Ionization Detector (51i-LT, Thermo Scientific, MA). WCS is maintained by the Santa Barbara County Air Pollution Control District. Daily instrument calibration occurs after midnight, rendering C unavailable 00:50 to 02:09 local time, LT. WCS was improved significantly in 2008 from 1-hour to 1-minute time resolution, which allowed far higher values of C and u due to the shorter averaging times. Data analysis uses custom routines as well as standard routines and functions in MATLAB (MathWorks, MA).

Deleted: detector

First, WCS data were quality controlled to remove all values of C during the daily calibration, as well as to interpolate neighboring values that were unrealistically low, i.e., C less than 1.6 ppm in the 1990s and 1.85 ppm in the 2000s. Data since 2008 were smoothed by nearest-neighbor averaging, yielding 3-minute time resolution. Data prior to 2008 were hourly and were not smoothed. Wind data were nearest-neighbor averaged after decomposing into north and east components, followed by recalculation of u and θ.

2.2 *In situ* marine surveys

Offshore *in situ* survey data were collected by the *F/V Double Bogey*, a 12-m, 9-ton, fishing vessel with a near waterline deck (~0.2 m) and low overall profile (cabin at ~2.2 m). A sonic anemometer (VMT700, Vaisala) was mounted on a 6.5-m tall, 5-cm (2") diameter aluminum mast and measured 3D winds. Continuous, CH_4 and CO_2 data were collected 5 Hz by a Cavity Enhanced Absorption Spectroscopy (CEAS) analyzer (FGGA, LGR Inc., San Jose, CA). Vessel location and time were from a Global Positioning System (GPS) at 1 Hz (19VX HVS, Garmin, KS). CH_4 and CO_2 calibration with a greenhouse gas air calibration standard (CH_4: 1.981 ppmv; CO_2: 404 ppmv, Scott Marin, CA, purchased 2015, Sigma Aldritch, St Louis, MO).

Data are real time integrated and visualized in Google Earth on a portable computer (Spectre360, HP) using custom software, written in MATLAB (MathWorks, MA), that is described elsewhere (Leifer, Melton, Fischer, et al., 2018; Leifer, Melton, Manish, & Leen, 2014; Leifer, Melton, Tratt, et al., 2018; Leifer et al., 2016). Real-time visualization

Deleted: for AutoMObile trace Gas (AMOG) Surveyor

Deleted: ,

facilitates adaptive surveys, wherein the survey route is modified based on real-time data to improve outcomes (Thompson et al., 2015) - in this case to facilitate plume tracking and to ensure transects were near orthogonal to the wind.

Accurate, absolute winds are calculated from relative winds after accounting for vessel motion and filtering for non-physical velocity changes due to GPS uncertainty (Leifer, Melton, Fischer, et al., 2018). Filtering removes transient winds that are not relevant to plume transport. The filter interpolates GPS positions flagged as unrealistic.

Whole air samples were collected in evacuated 2-liter stainless steel canisters, which were filled gently over ~1 minute from ~1 m above the sea surface. The filled canisters were analyzed in the Rowland/Blake laboratory at the University of California, Irvine for carbon monoxide, CO, CH_4, and C_2-C_7 organic compounds. Samples were analysed by a gas chromatography multi-column/detector analytical system utilizing flame ionization detection.

2.3 Seep plume emissions model

The plume inversion model is a three-step process (Leifer, Melton, Fischer, et al., 2018; Leifer, Melton, Tratt, et al., 2018; Leifer et al., 2016). Emissions from focused seep areas were derived from offshore data by first fitting Gaussian function(s) to orthogonal transect *C'* data, termed the data model. *C'* is relative to *C* outside the plume, derived by linear interpolation across the plume transect. The data model is derived by error minimization using a least-squares linear-regression analysis (Curve fitting toolbox, MathWorks, MA). Next, the Gaussian plume model (Eqn. S1; Supp. Figs. S1 and S2) is fit to the data model. Transect data are collected close to orthogonal to the wind direction and are projected in the wind direction onto an orthogonal plane. See Leifer, Melton, Tratt, et al. (2018) for a validation study of the plume inversion model by comparison with remote sensing-derived emissions (which are largely insensitive to transport). The study found *in situ* and remote-sensing derived emissions agreed within 11%.

2.4 Seep field emissions model

The inversion model is based on gridding the seep field into numerous small additive Gaussian plumes that represent the area emissions and was written in MATLAB (MathWorks, MA). This assumes that each sea-surface grid cell contributes a Gaussian plume, an assumption that was tested during an offshore survey that collected meteorology and *in situ* concentration data downwind of several active seep areas.

Deleted: with

Deleted: survey

The definition of an area source versus a point source depends on the relevant length scales – an area source is well approximated as a point-source plume if sufficiently downwind (far field), where the distance for "sufficiently downwind" depends on the area source dimensions and meteorological conditions. Whereas WCS is near field for the entire seep field plume, it is far field for the small plumes from each grid cell.

The area source was based on a Sept. 2005 sonar survey sonar return, ω, map (Fig. 1), see Leifer et al. (2010) for sonar survey details, data were re-analysed for this study. Simulations used sonar data gridded at a hybrid 22/56-m in a UTM coordinate system, with origin at WCS. Specifically, gaps in the 22-m map were filled from the 56-m map (Supp. Fig. S3). The probability distribution of ω was used to identify the noise level (Supp. Fig. S4) as in Leifer et al. (2010).

The model calculates a Gaussian plume for $E_{i,j}$ for grid cell i and j, for each grid cell with ω above noise. $C'_{Sim}(x,y)_{i,j}$ and for the observed wind-direction, θ, resolved wind, $u(\theta)$, for a typical Santa Barbara channel boundary layer, BL=250 m. The initial $E_{i,j}$ was calculated by scaling such that the integrated sonar return, $\int \omega(x,y)$, scales to E_A=1.5x10^5 m^3 dy^{-1}, i.e., E_B from Hornafius et al. (1999). The Gaussian plume is calculated in a Cartesian coordinate system (Supp. Fig. S5A), rotated to θ, and the interpolated linearly to double the spatial resolution. Then, the rotated plume is regridded to UTM coordinates using the ffgrid.m function (Supp. Fig. S5B). Interpolation removes gaps in the regridded plume map. Then, the regridded plume is renormalized to ensure total mass is conserved before and after these operations. Rotated regridded plumes are translated to the seep field grid and added, yielding $C'_{Sim}(x,y)$, which is the simulated seep field plume anomaly (Supp. Fig. S5C).

The model scans θ for the seep directions (110°<θ<330°) and calculates the simulated plume anomaly, $C'_{Sim}(\theta)$ at WCS, which is compared with the observed WCS concentration, $C'_{Obs}(\theta)$. Hereafter, C_{Obs} and C_{Sim} and their anomalies refer to values at WCS. $C'_{Obs}(\theta)$ is defined,

$$C'_{Obs}(\theta) = C_{Obs}(\theta) - \min(C_{Obs}(\theta)) \quad (1)$$

with the minimum typically from the west in a direction with no known seepage. Specifically, $C'_{Obs}(\theta)$ was calculated by subtracting the minimum in the annualized observed $C'_{Obs}(t,\theta)$ each year, t, after applying a 7-year running average.

Emissions from suburban communities, light industry, and commercial centers enhance $C'_{Obs}(\theta)$ for the northwest to northeast (~330-30°). These terrestrial emissions were removed by fitting a Gaussian function to $C'_{Obs}(\theta)$ for 330°<θ<30° with the residual yielding $C'_{Obs}(\theta)$. This only affected $C'_{Obs}(\theta)$ for overlapping directions corresponding to the fields' eastern edge.

Simulations were run at angular resolutions of 2°. Higher angular resolution produced small artifacts for the 22/56-m sonar grid while the 11-m sonar grid was overly sparse due to the distance between sonar tracks (Supp. Fig. S3A).

The source is the ω map in units of decibels, whereas emissions are in units of moles m^{-2} s^{-2}. Given that the relationship between ω and bubble density (emissions) is complex and non-linear (Leifer et al., 2017), there is poor agreement between $C'_{Sim}(\theta)$ and $C'_{Obs}(\theta)$. Thus, a correction function, $K(\theta)$, is applied to emissions for each grid cell along each θ, $E_{i,j}(\theta)$, and the model rerun. $K(\theta)$ is defined,

Deleted: are calculated
Deleted: (θ)
Deleted: in wind direction θ
Deleted: and
Deleted: $E_{i,j}$
Deleted: is
Deleted: :
Deleted: 350
Deleted: 70
Deleted: sectors
Deleted: Removal of these
Deleted: was
Deleted: map
Formatted: Font: Italic
Formatted: Font: Italic
Deleted: , $E(i,j)$,
Deleted: θ

$$K(\theta) = {C'_{Obs}(\theta)}\Big/{C'_{Sim}(\theta)} \quad (2)$$

Initially, $K(\theta) = 1$, but in subsequent iterations, $K(\theta)$ is scaled as in Eqn. 2. Because $K(\theta)$ weights closer seeps more than more distant seeps, a distance-varying correction function, $K(r,\theta)$, was calculated such that,

$$\int_{r=0}^{r=\infty} E_A(r,\theta) = \int_{r=0}^{r=\infty} K(r,\theta)\, E_A(r,\theta)\, dr \quad (3)$$

where r is distance from WCS. E_A from simulations for different northwards shifts of WCS were fit with a polynomial to derive the function form of $K(r)$. Accounting for off-axis plume contributions requires several iterations to achieve *Convergence*, which was defined,

$$Convergence = {\sum C'_{Sim}(\theta) \sum C'_{Obs}(\theta)}\Big/{\sum C'_{Obs}(\theta)} \quad (4)$$

Iterations continued to *Convergence* of 1% or better – typically 4 to 5 iterations. Simulations suggest wind veering, ψ, was important, which was implemented by calculating $C'(\theta)$ and assigning it to $C'(\theta + \psi)$.

3 Results

3.1 Offshore *in situ* surveys

An offshore COP seep field survey measured *in situ* C_{CH4} and u on 28 May 2016. Data were collected from the Santa Barbara harbor (~7.5 km east of the seep field, Fig. 2A; Supp. Fig. S6) to offshore Naples, several kilometers west of the seep field. Overall winds were easterly with an onshore component near Campus Point flowing onto UCSB and a broad (6-km wide) offshore flow west of COP that shifts to along coast near Naples (Fig. 2A, white arrows). Observed winds veered ~10° from east to the west sides of the seep field, roughly comparable to the shift in coastline orientation.

Plumes are apparent downwind of major seeps, with the largest plume associated with the Trilogy Seep (Fig 2B). Strong plumes also are evident downwind of the La Goleta Seep and Patch Seep. Notably, the Seep Tent Seep plume was very weak. The Seep Tent Seep was the dominant seep area in the COP seep field from its appearance in June 1973 (Boles, Clark, Leifer, & Washburn, 2001) until recent years.

Additionally, the offshore survey identified focused plumes from beyond the extent of the seep field's 2005-sonar map. Specifically in the Goleta Bay, which has been noted (Jordan et al., 2020), and offshore Haskell and Sands Beaches, an area with abandoned oil wells, and off Naples Point (Fig. 2A, red arrow).

Plume alkane *C'* were determined by the difference between two "background" air samples collected immediately outside the plume and three Trilogy Seep plume air samples. CH_4 was 88.5% of *THC*, with ethane, propane, and butane at 3.1%, 4.2%, and 2.8%, respectively, with pentane, hexane, and heptane at 1.11, 0.13, and 0.04%, respectively (Table 1). Mean *THC* molecular weight is 19.6 g $mole^{-1}$ based on a composition weighting. Branched alkanes were

Deleted: to adjust E_A in cells along θ

Deleted: Simulations

Deleted: that

Deleted: shifted

Deleted: northwards showed E_A varied

Deleted: nearly linearly with distance

Deleted: areas

Deleted: of

detected, with 2-methylpentane and 3-methylpentane comprising 0.21%, each, as well as simple aromatics, e.g., benzene and toluene, with concentrations of 78 and 18 ppm, respectively.

The observed wet gas fraction, $\sum_{n=2}^{5} C_n / \sum_{n=1}^{5} C_n$ was 0.11 indicating a thermogenic origin, i.e., greater than 0.05 (Abrams, 2017) - and thus derived from marine organic materials. Although the olefins ethene and ethyne were detectable at 0.02% and 0.004%, respectively, butene was not detected. These olefins primarily derive from microbial processes (Abrams, 2017), thus, the ethane/ethyne ratio of 6200 strongly indicates a thermogenic source (Bernard et al., 2001). Plume atmospheric CO_2 was elevated by 12 ppm, thus CO_2 was 18% of Total Carbon, *TC*, – defined *TC* = *THC*+CO_2+carbon monoxide, CO. CO was elevated minimally in the plume, just 2 ppb. Given that CO_2 completely dissolves from bubbles well before reaching the sea surface (Clark et al., 2010), this demonstrates efficient vertical transport of dissolved seep gases to the sea surface.

Plumes for the Trilogy Seeps, La Goleta Seep, and Seep Tent Seep were inverse Gaussian plume modeled to derive emissions for each plume. For the Trilogy Seeps, the average *u* across the plume was 5.9 m s^{-1}, insolation was full sun, and the source height was set at 25 m based on Trilogy's atmospheric plume being buoyant. Model surface concentrations for Trilogy B plume are shown in Fig 2B. The other two seeps are far less intense and used a 1-m source height.

E for Trilogy A was 1.28 Gg CH_4 yr^{-1} (5600 m^3 CH_4 d^{-1}), whereas Trilogy B and C contributed 0.06 and 0.07 Gg CH_4 yr^{-1}, respectively, for a total of 6200 CH_4 m^3 d^{-1}. Note, plume origins and the sonar seep bubble plume locations do not precisely match because the sonar map is for near the seabed, and currents deflect the bubble surfacing location, up to ~40 m. La Goleta Seep released 4000 m^3 CH_4 d^{-1} and the Seep Tent Seep released 310 m^3 CH_4 d^{-1} with almost no surface bubble expression. For comparison, Clark et al. (2010) used a flux buoy, which measures near surface bubble fluxes, and found Trilogy Seep emissions of 5500 and 4200 m^3 THC d^{-1} and 930 m^3 THC d^{-1} for La Goleta Seep in 2005 and 5700 m^3 THC d^{-1} for the Seep Tent Seep in 2002. During the cruise, surface bubble plumes were not observed for the Seep Tent Seep, although its bubble plume had been a perennial and dominant feature since its appearance. Note, Clark et al. (2010) reported *THC* in near sea surface bubbles was 91% CH_4.

3.2 West Campus Station

3.2.1 Temporal trends

WCS is 500 m from the coast (to the southwest) at 11-m altitude and 850 m almost due south to the 11-m altitude bluffs of Coal Oil Point (Fig. 1). Terrain slopes gently towards the coast to the southwest and towards a lagoon to the south-southeast, rising again to the southeast to the COP bluffs. This flat relief likely has small to negligible effect on wind speed and direction, although differential land-ocean heating could influence winds. Wind veering is likely for the coast to the east of COP due to the orientation of the coastline and bluffs.

Deleted: 0.078
Deleted: 0.180
Deleted: -
Deleted: also
Deleted: as
Deleted: 2A
Deleted: y
Deleted: y
Deleted: y
Deleted: ay
Deleted: y
Deleted: ay
Deleted: y

The WCS improvements in 2008 (Fig. 3-dashed line) allowed far higher values of C and u (Supp. Fig. S7A, S7B). Comparison of the probability distributions of u and C, $\phi(u)$ and $\phi(C)$, respectively, before and after the upgrade did not suggest biases were introduced (Supp. Fig. S7C, S7D). Specifically, changes in the average and median values and in the baseline after 2008 were from better measurement of higher value events (gusts and short positive C anomalies).

Significant daily, seasonal, and interannual variations are apparent in the day-averaged u and C (Fig. 3). The calmest season is late summer to fall, whereas spring is the windiest and most variable due to synoptic systems (Fig. 3A). Winds have strengthened since a minimum in 1995-1996, moreso for the seep directions with stronger winds becoming more frequent and moreso for summer than winter (Supp. Figs. S8, S9).

Trends in C reflect trends in both seep field emissions and ambient C. C is higher in fall and spring (Fig. 3B). Given that stronger winds decrease C through dilution, this suggests the seasonal variation in C underestimates the seasonal variation in emissions. Several studies have shown increased emissions under higher wave regimes (storminess), reviewed in Leifer (2019) and proposed from wave pumping. Storms increase evasion from higher wave turbulence and breaking-wave bubbles, which sparge dissolved CH_4 and other trace gases down to the seabed in shallow (<100 m) waters (Shakhova, Semiletov, Salyuk, et al., 2010). Note, u, θ, and C' correlate with time of day. For example, north generally reflects weak, offshore nocturnal winds with no seep contribution.

3.2.2 Spatial heterogeneity

Calculating the angular-resolved average C, $C_{ave}(\theta)$, for the complete dataset with respect to θ shows the highest C from the main seep field direction (155-250°, Fig. 4). For the seep directions, $C_{ave}(\theta)$ was poorly fit by a single Gaussian function but well fit (R^2 = 0.997) by two Gaussian functions with peaks at 178° and 198° corresponding to the Seep Tent and Trilogy Seeps' directions, respectively (Figs. 4A, 4B). Notably, the fit residual showed a linear increasing trend, $dC_{ave}(\theta)/d\theta$, of 0.17 ppb degree^{-1} from 180 to 210° (Supp. Fig. S9B) consistent with evasion from a dissolved downcurrent plume that drifts west-northwest along the coast (Leifer, 2019).

The average C anomaly, $C'_{ave}(\theta)$, was calculated from the average of $C_{Obs}(\theta)$, after Eqn. 1, with terrestrial anthropogenic sources to from the north to northeast removed. The minimum in $C_{Obs}(\theta)$ was at 270°, a direction with no mapped seepage that also is beyond the dissolved plume's approximate shoreward edge. Figs. 4A and 4B show $C_{Obs}(\theta)$ before removal of terrestrial emissions, which do not overlap in any significant manner with seep field emissions.

There is a strong, focused peak in $C_{max}(\theta)$ at $\theta \sim 190°$, close to the Seep Tent Seep direction (Figs. 4E, 4F), which is fairly isolated on the offshore seep trend (Fig. 1). This peak also is close to the direction of Tonya Seep on the inshore seep trend and to the small, unnamed area of seepage to the west of Trilogy Seep on the Red Mountain Fault trend.

Deleted: Ellwood
Deleted: Trend
Deleted: along

The θ-resolved maximum $C(\theta)$, $C_{max}(\theta)$, remains elevated through ~270°, far west of the $C_{ave}(\theta)$ peak at ~200°. This strongly suggests that the seep field extends further to the west-northwest than current maps. These data cannot be explained by dissolved plume outgassing, which would affect $C_{ave}(\theta)$ but not $C_{max}(\theta)$.

$C(\theta)$ enhancements for non-seep directions (Fig. 4A, 4B) show a peak at ~35°, corresponding to the direction of a commercial center amid suburban development. This could result from terrestrial seepage and natural gas pipeline leakage and/or *THC* emissions from communities and traffic.

Neglecting the synoptic system, topographic forcing from the east-west Santa Ynez Mtn. range means that the strongest winds are the prevailing westerlies (Fig. 4C, 4D). North winds (320-15°) largely are weak as are winds from due south; however, the sea breeze strengthens winds rapidly away from due south. θ peaks in the maximum winds (1-minute sustained), $u_{max}(\theta)$, correspond to the west and east peaks in $u_{ave}(\theta)$ with strengths to 16 m s^{-1}. Interestingly, there also are strong north (0-30°) winds or downslope flow, termed sundowner winds, a highly localized and infrequent phenomenon. The overlap of $u_{med}(\theta)$ and $u_{ave}(\theta)$ shows winds largely are normally distributed.

The median C, $C_{med}(\theta)$, and average C, $C_{ave}(\theta)$, have similar shapes, albeit with lower values at all θ (Fig. 4A), indicating C is not normally distributed. This is shown in the wind direction-resolved wind speed probability distribution, $\phi(\theta,u)$ (Fig. 5A), defined such that

$$\int \phi(\theta,u)du = 1, \quad \int \phi(\theta,C)dC = 1. \tag{5}$$

$\phi(\theta,u)$ is very narrow (y-axis) for the northeast (~45°) where winds are largely weak and broad for the east-southeast (70-135°) and the prevailing westerlies (250-280°). The east-southeast distribution skews to the south (stronger winds extend further from the south - offshore), whereas the prevailing westerly wind distribution skews to the northeast (as does the coastline).

In the seep direction, $\phi(C,\theta)$ extends to much higher values than from non-seep directions (Fig. 5B). $\phi(C,\theta)$ is asymmetric with θ extending further to the west than the seep field extent (240°) and then decreasing more abruptly than the decrease to the east. This asymmetry is expected given the seep field's asymmetric orientation relative to WCS (eastern seepage is more distant). Emissions beyond the field's mapped western edge arise from downcurrent plume outgassing and potentially contributions from unmapped seeps.

3.2.3 Seep field diurnal emissions cycle

C and u for the seep field direction, u_{seep}, and C_{seep}, respectively, follow diurnal patterns that are not the same as the overall diurnal pattern due to the wind direction constraint and because C_{seep} depends on u_{seep}. The dependency arises because higher u dilutes emissions, decreasing C, but higher u also increases dissolved plume evasion and bubble-mediated emissions from higher swell (after a delay for wave build-up). Diurnal winds in coastal regions feature a

Deleted: winds are
Deleted: and are the strongest
Deleted: buildup

shift between weak nocturnal offshore winds that veer to onshore winds in the morning - the sea breeze circulation. This was explored in time and direction segregated u and C and seep direction averaged u_{seep} and C_{seep} for 90-270° (Fig. 6). Data were segregated by θ for pre- and post-2008 (when station improvements facilitated better wind characterization, particularly for night winds, which are seldom from the seep field direction, see Supp. Fig. S10 for 1991-2007). $u(\theta,t)$ and $C(\theta,t)$ were 2D Gaussian kernel smoothed with a 1-bin standard deviation (contours based on a 3-bin standard deviation) by the imgaussfilt.m algorithm (MATLAB, MathWorks, MA) after interpolating the calibration data gap 24:00-01:00.

Early morning (01:00–03:00) u_{seep} are stronger because typical nocturnal winds are northerlies (land breeze), coming from the south largely during storms. These are accompanied by elevated C_{seep} implying greater emissions despite enhanced dilution from stronger winds. The minimum in both u_{seep} and C_{seep} occur in the early morning (04:00-08:00), with both increasing slightly through midday (~12:00). C_{seep} follows an afternoon trend of an overall decrease to a minimum at ~20:00 before increasing into the late evening.

Underlying these trends are complex temporal spatial patterns. u for the north to northeast reaches a maximum around noon and peak around 16:00; while C for northeast to east is low in the morning reaching a peak to the east in the afternoon and likely reflects terrestrial sources. This pattern in $C(t,\theta)$ extends to nearly 130°. Beyond the seep field's western edge, u is elevated from the prevailing direction (270°) with C elevated throughout the morning. There also is a short-lived peak in u around noon at ~300°, which corresponds to a short-lived depressed C. These could be consistent with wave development time, transport time, and sparging of the downcurrent plume; however, interpretation based on these patterns largely is speculative.

3.3 Overall seep field emissions

3.3.1 Overall emissions

Average atmospheric emissions, E_A, for 1990-2020 were derived by an iterative Gaussian plume model, initialized with the 2005 sonar map (Fig. 7A). An emissions sensitivity study on the effect of grid resolution was conducted for resolutions from 11 to 225 m and a 22/56-m hybrid grid (Supp. Fig. S3). Simulations used moderate insolation to derive the turbulence parameters and stability class (Supp. Fig. S2), a 250-m BL, typical of Santa Barbara Channel marine values (Edinger, 1959; Rahn, Parish, & Leon, 2017), and 2° angular resolution (Hanna et al., 1982). Simulations were run iteratively until convergence, typically within 5 iterations (Supp. Fig. S11). Sensitivity studies found the distance weighting function, $K(r,\theta)$, was linear (Supp. Fig. S12).

Simulations could not reproduce observations in the Platform Holly direction (θ=238°). Thus, a source was added for the platform area, which improved simulation-observational agreement in this wind direction. Since significant seep bubbles plumes generally are not observed in the platform's vicinity, these emissions could arise from incomplete combustion during flaring.

Deleted: ,

Deleted: ,

Deleted: from

The model-derived, E_A, for 1990-2020 was 83,400 m^3 d^{-1} (Fig. 7). Using a composition-weighted *THC* molecular mass of 19.6 g $mole^{-1}$ implies 27 Gg *THC* yr^{-1}. Atmospheric seep gas is 88.5% CH_4, implying 19 Gg CH_4 yr^{-1} seep emissions (Table 1). Given that CH_4 is 73% of *THC*, non-methane hydrocarbon (NMHC: C_2-C_7) emissions are 9,600 m^3 d^{-1} and gases emissions of 6.0 Gg yr^{-1}. For reference, Santa Barbara County 2018 Reactive Organic Carbon (ROC) emissions are listed at ~27 tons d^{-1} (9.9 Gg yr^{-1}) (ourair.org/emissions-inventory, SBAPCD). For our analysis NMHC and ROC are the same. The largest NMHC was propane with emissions of 3510 m^3 d^{-1}, followed by ethane at 2590 m^3 d^{-1}. The NMHC components of *THC* are conservative (do not react significantly) on the typical transport timescales from the seep field to WCS (20-30 minutes).

Seabed emissions, E_B, are necessarily significantly greater than E_A as E_A misses the fraction of emissions that remain in the water column, E_W, at least in the field's near downcurrent. There are two notes, the model E_A includes evasion from the dissolved plume in the area covered by the seep field sonar map. Secondly, the model does not include E_A from the dissolved fraction that evades beyond the seep field extent. For the seep field area and near downcurrent area, Clark et al. (2000) estimated a 50:50 air/water partitioning based on a field study, implying E_B = 167,000 m^3 d^{-1} for 1990-2020 (54 Gg yr^{-1}). A comparison of E_A versus ω showed a very steep increase with ω for E_A = 1-10 g s^{-1} m^{-2} with rollover at ω~0.022 (Supp. Fig. S13), which was approximately the noise level (Supp. Fig. S4).

Insights were provided by how the model partitioned emissions between different seep areas (Fig. 7). Particularly notable is the model's treatment of the Trilogy Seep area - the second strongest seep area after the Seep Tent Seep during the study period. The model re-assigned Trilogy Seep emissions to seepage to the west, representing Trilogy Seep emissions as unrealistically weaker than other, smaller seeps, such as IV Super Seep. One likely contributor to this re-assignment is wind veering (Supp. Fig. S14). Also suggesting wind veering is the model's assignment of strong emissions to the field's eastern and western edges despite weak sonar returns. In a comparison of the Seep Tent Seep and La Goleta Seep areas, the model emphasized the Seep Tent Seep whereas La Goleta Seep emissions were shifted to inshore seepage. This re-partitioning was greatly reduced for a +10° wind veer, which also lessened the strengthening of emissions from the field's western edge relative to sonar. Given the lack of field data between the seep field and WCS on wind veering, further wind veering analysis was not conducted.

3.3.2 Seep field sector emissions

To investigate sub-field scale emissions, the seep field was segregated into three sectors: inshore, offshore east, and offshore west (Fig. 1). Based on integrating sonar return, ω, inshore seepage contributes 40% of the field's ω with the offshore seep trend split between 9% for the west and 51% for the east. Supporting this comparison is the similarity in the normalized sonar return probability distribution, $\phi_n(\omega)$, for the inshore seeps and offshore east seeps (Fig. 8). In contrast, $\phi_n(\omega)$ for offshore west seepage differed dramatically despite the similarity in geology along the anticline underlying the offshore seep trend (Leifer et al., 2010). This likely results in part from the interaction between

Deleted: 500
Deleted: y
Deleted: y
Deleted: - ROC are organic species excluding CH_4 including alkanes and aromatic compounds
Deleted: y
Deleted: y
Deleted: y
Formatted: Font: Italic
Deleted: the
Deleted: seabed emissions,
Deleted: 1990-2020 of
Deleted: y
Deleted: or
Deleted: over
Deleted: 1990-2020
Deleted: the
Deleted: the

migration and production from Platform Holly. Although the normalized atmospheric emissions probability distribution, $\phi_n(E_A)$, for the inshore and offshore seeps are similar over most of the range (except the weakest, E_A<0.02 g s^{-1}), significant differences are evident between offshore east and west seepage. Offshore east seepage is more dispersed and favors weaker seepage compared to offshore west seepage.

The weakest seepage (ω<0.02) contributes negligibly to overall sonar return and had no notable inshore-offshore $\phi_n(\omega)$ difference (Fig. 8). The largest difference is between the strongest seepage (ω>0.5) for the inshore and offshore seeps. Specifically, there is a strong peak at ω~0.45 and nothing stronger for the inshore seeps, whereas offshore $\phi_n(\omega)$ continued to ω~0.7. The E_A probability distribution, $\phi_n(E_A)$, for the strongest inshore seepage was similar to $\phi_n(E_A)$ for strong offshore seepage. However, this masked a significant east-west offshore seepage difference. Specifically, $\phi_n(E_A)$ for strong seepage was reduced far more for offshore east seepage than offshore west seepage, and the reverse for weak seepage.

The similarities of these distributions suggest that the controlling geological structures (fractures, fault damage zones, chimneys, etc.) are the same for inshore seepage and offshore east seepage, with the primary difference for the strongest seepage in these two sectors which are of similar strength – the inshore Trilogy Seeps provide focused emissions, whereas the offshore east La Goleta Seeps are comparatively dispersed and far oilier.

Although, ω is not E_A, E_A followed the 40:60 partition in ω between inshore and offshore seepage. Interestingly, the E_A partitioning between the offshore east and offshore west differed significantly from sonar partitioning with 21% of E_A from offshore west and 38% from offshore east. This greatly accentuated the E_A Seep Tent Seep area. In part, this arises from a diurnal cycle bias – WCS observes the offshore west seeps for afternoon/evening westerly winds, which are stronger, whereas WCS observes the offshore east seeps when winds are weaker, earlier in the day (Fig. 6B). Winds increase bubble emissions from wave hydrostatic pumping and dissolved gas evasion. Also potentially contributing is saturation of ω at very high bubble-density bubble plumes, such as the Seep Tent Seep and Trilogy Seep (Leifer et al., 2017). Saturation would imply an under-estimate of ω for the strongest seep area emissions which are for the west offshore seepage, altering the west:east ω ratio (9%:51%).

3.3.3 Uncertainty and emissions sensitivity

Given the number of sources with poorly characterized variability, uncertainty is best assessed by Monte Carlo simulations; however, this was unfeasible due to the simulations' computational demands. Thus, emissions uncertainty was investigated by sensitivity studies (**Fig. 9**). Where data were available, uncertainty due to a specific parameter was estimated from the data. Specific parameters studied included sonar resolution, angular resolution, $\delta\theta$, wind speed, u, concentration anomaly, C', boundary layer height, BL, wind veering, ψ, spatial northing offset, Y, and the inshore and offshore seepage partitioning, ζ. Sensitivity study details are presented in Supp. Sec. S7.4.

Deleted: and compared to $\phi_n(\omega)$

Deleted: se

Deleted: and

Deleted: in the capping Sisquoc Formation

The contribution to uncertainty from $\delta\theta$, C', ψ, and spatial offsets within the seep trends were minimal – just a few percent or less. Moderate uncertainty was identified for BL and ζ. For example, for BL ranging from 150 to 350 m, mean E_A uncertainty was 6%. Although u has strong sensitivity, combined with BL it does not as u counters BL – lower u corresponds to higher BL. There still is uncertainty, though in the value of BL, which is not measured. Assessing uncertainty in ζ was more challenging as there is no verification data on variability in the E_A partitioning between the inshore and offshore seep trends. The mean E_A uncertainty for $-50\% < \zeta < 50\%$ is 11.5% from a polynomial fit. Still, the consistency in seepage location between sonar surveys spanning decades (Leifer, 2019) suggests only modest changes in ζ over the multi-decade time period of model averaging. Total uncertainty was taken as 15% based on the sum of uncertainty in BL and ζ, each averaged to the nearest 5%.

3.4 Ellwood Field emissions

$C(\theta)$ increases to the northeast with a peak at 290-320° corresponding to the direction towards abandoned wells off Haskell Beach (Fig. 10). Emissions from this area – either from natural seepage or leaking wells – were noted in the offshore survey data near Haskell Beach (Fig. 2A). Additionally, $C_{max}(\theta)$ shows a 22-ppm peak in in this direction well above $C_{ave}(\theta)$ (Fig. 4F), consistent with transient releases from natural seep and/or abandoned well emissions.

Ellwood field production continued through the 1970s with wells drilled into the geological structures that allowed oil accumulation (Olson, 1983) including faults that provide migration pathways (Leifer et al., 2010). There are many abandoned wells from these oil fields and from others fields on the Goleta Plains, beaches, and shallow near-coastal waters to the west-northwest of WCS (offshore Haskell Beach and onshore around Naples Point). Currently, active wells only are found at the La Goleta Gas field (a natural gas storage field), east of WCS.

Deleted: ;

Faults associated with these anticlines provide migration pathways and are approximately aligned with the coast in a series of roughly parallel faults extending onshore (Minor et al., 2009). The onshore/coastal Ellwood field (northwest of the South Ellwood field) sources from the primarily sandstone Vaqueros Formation (Olson, 1983), whose main trap is an anticline at the western edge of the North Branch Western More Ranch Fault (NBWMRF). Offshore seepage tracks some of these faults, e.g., the Isla Vista Fault trend corresponds to an offshore seep trend in Goleta Bay that includes the Goleta Pier Seep, whereas wells follow the NBWMRF trend offshore of Haskell Beach.

4 Discussion

4.1 Atmospheric seep field observations

4.1.1. Air quality station

A range of approaches are available to evaluate marine seepage CH_4 emissions: *in situ* approaches including direct capture (Leifer, 2015; Washburn, Johnson, Gotschalk, & Egland, 2001), fluid flow measurements (Leifer & Boles, 2005), video (Leifer, 2015), and remote sensing approaches that include active acoustics, i.e., sonar (Hornafius et al., 1999), dissolved *in situ* (Marinaro et al., 2006), and passive acoustics (Wiggins et al., 2015). Remote sensing is the best approach for long-term monitoring to capture shifts in emissions between vents. To date, only sonar remote sensing has provided quantitative seep plume (seabed) emissions. Notably, sonar ranges are up to a few hundred meters, far less than the size scales of many seep fields, whereas high power demands typically require a cabled observatory for long-term observations.

This study demonstrated that air quality station data can provide the long-term continuous data needed to capture seasonal variations including emissions during storms and transient events, which field campaigns likely miss. For example, sonar surveys generally are scheduled during summer when seas are calmer and winds more predictable and when seepage is weakest (Fig. 3); however, not during storms when emissions likely are enhanced.

The approach derived atmospheric trace gas emissions for a dispersed area source constrained by sonar seepage maps from long-term air quality and meteorology data. This approach can be extended to terrestrial seepage if the source can be constrained spatially (due to geology); although nearby anthropogenic sources may complicate emissions assessments. Other terrestrial sources such as landfills, O&G production fields, or industrial sites – if spatially constrained – could be addressed by this approach, particularly if isolated from other confounding sources. The use of cavity enhanced absorption spectrometers that can speciate gases like CH_4 and C_2H_6 that could enable discrimination some confounding sources as well as better characterization of emissions. Although an onshore station can address nearshore seepage, further offshore seepage could be addressed by a moored station. Moored stations also could include *in situ* aqueous chemical sensors, current measurements.

4.1.2 *In situ* atmospheric surface surveys

Atmospheric emissions were assessed for three seep areas - zone of focused seepage - by an atmospheric *in situ* survey approach wherein downwind data are collected orthogonal to the wind direction in a transect that spans the plume (background to background on the plume's edges). This approach was developed for terrestrial sources (Leifer, Melton, Tratt, et al., 2018) yet remains unused for offshore marine seepage, which often are area sources. In this study, this was addressed by gridding the area source and treating each grid as a far-field point source. Gaussian plume inversion requires distant source(s), i.e., far field. Downwind *in situ* transects of three strong seep areas all were well characterized by the Gaussian plume model.

Deleted: while

Deleted: -

Deleted: tend

Deleted: to occur

Deleted: Surveys

Formatted: Font: Italic

One advantage of atmospheric surveys is rapidity - a single transect of a few minutes is sufficient to derive emissions for a seep area. In comparison, a flux buoy survey can require many hours to a day (Clark et al., 2010), during which forcing factors (waves, tides, etc.) change significantly. Also rapid are seep area sonar surveys (Wilson, Leifer, & Maillard, 2015) allowing a combined sonar and atmospheric survey to repeat characterize emissions and sea-air partitioning within a few hours. With respect to the entire COP seep field, whereas a sonar survey requires two to three days (Leifer et al., 2010), a downwind atmospheric survey is far more rapid, requiring perhaps an hour. This allows repeat field emissions measurements over a tidal cycle.

4.2 Seep field emissions

4.2.1 Total emissions

To date, only two estimates of COP seep field seabed emissions, E_B, have been published. Hornafius et al. (1999) estimated E_B=1.5x10^5 m^3 dy^{-1} (64 Gg yr^{-1}) based on sonar surveys covering 18 km^2 from Nov. 1994 – Sep. 1996, collected during the summer to late fall seasons. This value excluded Seep Tent collection. A 4.1 km^2 sonar survey in Aug.-Sep. 2016 estimated E_B=24,000 m^3 dy^{-1} (Padilla, Loranger, Kinnaman, Valentine, & Weber, 2019), significantly lower, which in part arises from field subsampling, but also could arise from long-term changes; however, neither study addressed temporal variability. The sonar surveys occurred in summer and fall when seepage activity is at a minimum, whereas winter and early spring feature much higher activity associated with large transient events and storms (Bradley et al., 2010).

Hornafius et al. (1999) used an engineered bubble plume to calibrate emissions, an approach also used in Leifer et al. (2017). Due to technology limitations at the time, the strongest seepage was clipped or saturated, i.e., underestimated, and the survey did not cover shallow seepage. Thus, the Hornafius et al. (1999) emissions estimate is a lower limit for summer/fall emissions. The Padilla et al. (2019) survey was calibrated by an inverted seep flux buoy suspended at 23 m. This differs significantly from the seep flux buoy measurement approach reported in Washburn et al. (2001), which are collected in surface drift mode. Surface drift mode ensures a horizontal orientation for the buoy and an absence of lateral velocity difference between the capture device and currents – either of which decreases capture efficiency from 100%, biasing derived emissions low. Further, the Padilla et al. (2019) survey was calibrated 1 month after the sonar surveys, whereas the 1995 engineered plume calibration by Hornafius et al. (1999) was contemporaneous. The Hornafius et al. (1999) approach accounts in part for dissolution between the seabed and survey depth window - it used air rather than CH_4, which dissolves slower than CH_4. Dissolution losses for CH_4 between the seabed and the depth window can be addressed by a numerical bubble model (Leifer et al., 2017).

The Gaussian plume model-derived E_A was 8.3x10^4 m^3 dy^{-1}. Based on the Clark et al. (2000) assessment that half the seabed seepage reaches the atmosphere, E_B=1.7x10^5 m^3 dy^{-1}; very similar to E_B=1.5x10^5 m^3 dy^{-1} from Hornafius et al.

Deleted: s

Deleted: (partially)

Deleted: ,

Deleted: albeit

Deleted: air

Deleted: methane

Formatted: Subscript

(1999). This agreement is coincidental as it neglects seasonal and interannual trends. For example, Bradley et al. (2010) found 1994-1996 emissions were well below the average for 1990-2008, increasing significantly after 2008.

4.2.2 Methane and non-methane hydrocarbon emissions

Analysis of atmospheric samples provided a picture of the complexity of atmospheric emissions that arises from the multiple pathways underlying atmospheric emissions. Specifically, as bubbles rise, they lose lighter and more soluble gases faster (deeper in the water column), leading to differences between evasion from dissolved gases and direct bubble transport (Leifer & Clark, 2002). Thus, bubble-mediated transport enhances larger alkanes relative to smaller alkanes leaving more of the smaller alkanes in the water column. For strong seeps, bubble plumes are associated with strong upwelling flows (Leifer et al., 2009), which transport dissolved gases to the sea surface where they outgas. Additionally, oil (as droplets and bubble coatings) enhances alkane transport due to slower dissolution and diffusion of larger alkanes through oil.

Atmospheric plume concentrations were 11.5% *NMHC* and 88.5% CH_4, very similar to Hornafius et al. (1999) who referenced the Seep Tent composition (88% CH_4, 10% *NMHC*, and 2% nitrogen) as very similar to the reservoir composition. Note, Clark et al. (2010) observed Trilogy near sea surface bubbles with 5.7% to 7.9% *NMHC* and 52.4 to 79.7% CH_4, demonstrating significant partitioning. The similarity between the atmospheric and seabed composition despite the difference in the bubble composition demonstrates efficient dissolved gas transfer to the sea surface.

COP seep field seabed emissions are orders of magnitude greater than typically reported for other seep areas, e.g., summary Römer et al. (2017) where emissions for 12 different seep areas including sites in the North Sea, Pacific northwest, Gulf of Mexico, etc., were 2-480 tons yr^{-1}, multiple orders of magnitude less than COP seep field seabed emissions. Römer et al. (2017) used a bubble model for Dogger Bank seepage in the North Sea to estimate emissions for observed atmospheric CH_4 plumes. The model estimated direct atmospheric bubble-mediated emissions of 21.7 ton yr^{-1}, 20% of seabed emissions. For the Tommelieten Seeps (in 70-m water) Schneider von Deimling et al. (2011) estimated 4% of the 0.024 Gg CH_4 yr^{-1} seabed emissions, i.e., ~1 Mg CH_4 yr^{-1} reached the atmosphere by bubble-mediated transfer. Schneider von Deimling et al. (2011) used a bubble model based on an assumed bubble size and neglected diffusive flux. These diffusive fluxes include bubble dissolution into the wave mixed layer in the local area. A few studies have directly measured atmospheric fluxes by an air-sea gas transfer model. For example, Schmale, Beaubien, Rehder, Greinert, and Lonmbardi (2010) found seep air fluxes of 0.96-2.32 nmol m^{-2} s^{-1}, much higher than the ambient Black Sea flux of 0.32-0.77 nmol m^{-2} s^{-1}. In the Black Sea, ambient emissions arise from microbially produced CH_4 in shelf and slope sediments (Reeburgh et al., 1991). Di, Feng, and Chen (2019) estimated 7.7 nmol m^{-2} s^{-1} for the shallow South China Sea based on an air-sea gas transfer model. If we disperse COP seep field atmospheric emissions of 1.15×10^9 M yr^{-1} over the ~6.3 km^2 of 25x25 m^2 bins with emissions, we find 5.7 µM m^{-2} s^{-1}, three orders of magnitude greater.

Recent estimates of total global geo-CH_4 sources from a bottom-up approach are 45 Tg yr^{-1} with submarine seepage contributing 7 Tg yr^{-1} (Etiope & Schwietzke, 2019), implying COP seep field contributes ~0.27% of global submarine emissions. However, an estimate of pre-industrial CH_4 emissions (not confounded with fossil fuel production emissions) based on ice core $^{14}CH_4$ suggested 1.6 Tg geo-CH_4 yr^{-1} emissions (Hmiel et al., 2020). This estimate, if accurate, would imply the COP seep field contributes an astounding 1% of global seep emissions (submarine and aerial) and is difficult to reconcile with the COP seep field and other top seepage estimates. For example, CH_4 atmospheric emissions for the Lusi hydrothermal system of 0.1 Tg yr^{-1} (Mazzini et al., 2021), a hotspot in the Laptev Sea of 0.9 Tg yr^{-1} into shallow seas (Shakhova, Semiletov, Leifer, et al., 2010), and for the East Siberian Arctic Sea using eddy covariance of 3.0 Tg yr^{-1}(Thornton et al., 2020). Thus, COP seep field emissions either play a significant role in global seep emissions or indicate that geo-gas emissions are less tightly constrained.

COP seep field C_2H_6 emissions were 1.27 Gg C_2H_6 yr^{-1}. For reference, this is 11% of the 11.4 Gg C_2H_6 yr^{-1} in 2010 for the South Coast Air Basin (SCAB), which includes Los Angeles (Peischl et al., 2013). Globally, Simpson et al. (2012) and Höglund-Isaksson (2017) found 11.3 and 9.7 Tg C_2H_6 yr^{-1} in 2010, respectively. C_2H_6 has been increasing since 2010 due to increased O&G production emissions (Helmig et al., 2016). Globally, seeps are estimated to contribute 2-4 Tg C_2H_6 yr^{-1} (Etiope & Ciccioli, 2009), and from ice cores, 2.2-3.5 Tg yr^{-1} {Nicewonger, 2016 #3816}. This suggests the COP seep field contributes 0.03-0.06% of global seep emissions.

Seep THC was 4.2% propane, implying emissions of 2.5 Gg C_3H_8 yr^{-1}. Global propane emissions are 10.5 Tg yr^{-1} (Pozzer et al., 2010), with 1-2 Tg yr^{-1} estimated for seeps (Etiope & Ciccioli, 2009). This suggests the COP seep field contributes 0.05-0.1% of the global seep budget. Oceans are estimated to contribute 0.35 Tg C_3H_8 yr^{-1} (Pozzer et al., 2010), less than geological seepage contribution.

Based on an evaluation of the COP seep field emissions with respect to global seep ethane and propane emissions, COP seep field contribution to global geo-CH_4 emissions are consistent with recent global geo-gas CH_4 emissions estimates of 45 Tg yr^{-1} (0.04%) (Etiope et al., 2019), not the significantly lower pre-industrial estimates of global geo-CH_4 emissions, e.g., 1.6 Tg yr^{-1} (1.15%) (Hmiel et al., 2020).

Global butane emissions are 14 Tg C_4H_{10} yr^{-1} (Pozzer et al., 2010), higher than ethane and propane. COP seep field butane (C_4) and pentane (C_5) emissions were 2.2 Gg C_4H_{10} yr^{-1} and 1.1 Gg C_5H_{12} yr^{-1}, respectively, with combined C_2-C_5 emissions of 7.1 Gg yr^{-1}, compared to 65 Gg yr^{-1} from the entire SCAB, i.e., COP seep field contributes ~5% the SCAB. COP C_2-C_5 emissions are significantly above that of the La Brea area, estimated at 1.7 Gg yr^{-1} (D. Weber et al., 2017). Note, COP seep field atmospheric C_2-C_5 emissions certainly are larger, potentially significantly, as larger alkanes also are emitted from oil slicks but were not considered for this study, and furthermore, the atmospheric plume from the slicks was not sampled for this study.

Deleted: 25
Deleted: the
Deleted: bottom-up

Both benzene and toluene were detected with estimated emissions of 8300 and 2300 kg yr^{-1}, respectively. These emissions likely are underestimates, potentially significantly, due to neglecting the oil slick evaporation contribution. Both gases are of significant health concerns, as are alkanes like pentane and hexane.

4.3 Downcurrent emissions

The seep field concentration, $C'(\theta)$, anomaly was centered at θ~200° and well matched the location of the seep field, and moreover, was well described by a dual Gaussian function (**Fig. 4B**). This was surprising given that the seep field is asymmetric with respect to a 200° axial line from WCS to COP. Underlying this seeming discrepancy is that WCS winds are weakest from due south and strongest from the west (prevailing) and also stronger to the east-southeast (**Fig. 4C**).

The residual of the Gaussian fit increased in the downcurrent direction (**Supp. Fig. S9B**), consistent with evasion from the downcurrent dissolved plume and seepage from this area. The dissolved plume roughly follows the coast, extending as far as ~280° from WCS due to the coastline shift from northwest to west around Haskell Beach (**Fig. 10**), ~30° beyond the seep field's sonar mapped western edge (**Fig. 1**). As prevailing winds are westerlies (paralleling the coastal mountains), downcurrent plume evasions decrease with distance due to dispersion and also as surface waters become depleted by evasion. Evasion increases non-linearly with u, particularly for winds that include wave breaking (Nightingale et al., 2000); however, higher winds also dilute emissions. Note, there are no mapped seeps in this area.

Deleted: 2

Dissolved plume emissions also likely occur from east of the field, leading the model to emphasize seepage at the field's eastern extent, too. Specifically, strong prevailing afternoon westerly surface winds drive a near-surface dissolved plume eastwards. When these westerly winds calm down late in the evening, easterly winds transport evasion from this east-displaced dissolved plume towards WCS. Additionally, it also is possible that the COP seep field extends further east than mapped in sonar surveys, at least during some seasons.

4.4 Focused seep area emissions

Trilogy Seep area emissions were estimated at 6,200 m^3 CH_4 dy^{-1} in May 2016. For comparison, Clark et al. (2010) found 5500 and 4200 m^3 THC dy^{-1} (4,900 and 3,700 m^3 CH_4 dy^{-1}) for Trilogy Seep as measured by flux buoy for near surface bubble fluxes in Sept. 2005. Note, the plume inversion approach also includes outgassing of near surface waters that have enhanced C_{CH4} from plume dissolution, which the flux buoy approach does not include. Although Clark et al. (2010) found surface bubbles had undetectable CO_2, the atmospheric plume's CO_2 to CH_4 concentration ratio was comparable to the seabed bubble concentration ratio. This demonstrates significant upwelling flow transport of seabed water to the sea surface where dissolved gases evade near where the bubble plume surfaces. This near-plume evasion contributes to the atmospheric plume. Note, these emissions neglect downcurrent emissions. A 50:50

atmosphere:ocean partitioning suggests 2016 Trilogy Seep emissions were ~40% lower than in 2005 – a difference within the difference between the two 2005 Trilogy Seep measurements Clark et al. (2010).

In contrast, agreement was very poor for the Seep Tent Seep, for which Clark et al. (2010) mapped emissions of 5700 m^3 day^{-1} (5000 m^3 CH_4 day^{-1}) in Nov. 2002 whereas this study found 310 m^3 CH_4 dy^{-1}. This discrepancy was readily apparent with almost no visible surface bubble expression in May 2016, whereas the Seep Tent Seep has been a perennial feature since its appearance. The absence of more than a few scattered bubbles at the sea surface (the boil in 2000 was driven by a 1-2 m s^{-1} upwelling - Leifer, Clark, and Chen (2000) - indicates that most emissions are from evasion. A buoyancy plume associated with the rising oil (thick oil slicks surface above the Seep Tents) as well as CH_4 dissolved in the oil likely are transporting the observed, focused CH_4 emissions.

Deleted: methane

This is remarkable given that the seep field's geofluid migration "center" in recent decades has been the Seep Tent Seep (Bradley et al., 2010), which was the largest seep in the field in 2010 (Clark et al., 2010). The Seep Tent Seep consists of emissions not captured by the Seep Tents – two large (33-m square) steel capture tents on the seafloor. For reference, the Seep Tents captured ~16,800 m^3 gas dy^{-1} in the early 2000s (Boles et al., 2001). Bradley et al. (2010) found in WCS data that when overall seep field emissions decreased to a minimum in 1995, they were focused on the Seep Tent Seep direction. Note, the Seep Tent Seep was observed first in 1970 as a boil visible from 1.6-km distant. The Seep Tent seep was tented in Sept. 1982 (Boles et al., 2001).

Deleted: seepage

Underlying these observations are several factors. First, the Seep Tent Seep is modern – since 1978 – as it was not mapped in a 1953 seep survey (Leifer, 2019). At the time it was first reported as a sea boil visible over a kilometer distant (Boles et al., 2001). Since installation, overall Seep Tent production has diminished (Boles et al., 2001) by a factor of 3 from 1984 to 1995. Some fraction of this trend could have resulted from the expansion of active seepage beyond the seep tents. Perhaps more significantly, the Seep Tent Seep lies over one of the Platform Holly wells (Leifer et al., 2010; Fig. 3C), creating the potential of linkage between well production (including stimulation) and Seep Tent production and thus Seep Tent seepage (the uncaptured portion).

4.6 Diurnal trend and bias

The diurnal wind patterns typical of the coastal Pacific marine environment are weak offshore (northerly) night winds that shift to from the east in the morning and then swing to from the south. In afternoon they strengthen and shift to prevailing westerlies, continuing to late in the evening (Bradley et al., 2010). Note, WCS seep emissions require winds to "probe or scan" across the seep field, and thus miss the strong afternoon prevailing winds when emissions are expected to be higher. This is because higher wind speeds increase sea-air gas emissions of dissolved near-surface gases (Nightingale et al., 2000) and increase emissions from higher hydrostatic pressure fluctuation driven by wave height (Leifer & Boles, 2005). Given that prevailing winds are westerlies, higher afternoon emissions will generally (but not always) drift eastwards, missing WCS.

The diurnal wind pattern from the seep field direction is different from the overall (direction-independent) diurnal pattern. Typical nocturnal winds are quite weak, 1.5–1.7 m s^{-1} (**Fig. 6**). The strongest diurnal wind change was from late night to morning, a 20% decrease. Onshore winds (seep direction) in the middle of the night are from synoptic systems and were associated with the highest C'. Winds increase by a few percent to an early afternoon peak, decreasing through early evening before increasing again later in the night.

The diurnal trend for C from the seep direction followed the diurnal wind cycle, increasing by ~20 ppb and peaking ~2 hours later in the day than winds (15:00 versus 13:00 for C compared to u, respectively). This may reflect the lag in wave development with respect to wind strengthening and transport time. Based on sensitivity studies, the diurnal cycles in u and C correspond to variations of ~7% and ~9% in E_A.

Although efforts were made to characterize the diurnal cycle from WCS data, WCS data poorly sample the seep field for the higher wind speeds that occur in the afternoon which primarily are westerlies. Note, non-linearity in sea-air evasion with u means the model use of average u underestimates E_A. Thus, the contribution of the prevailing afternoon winds to diurnal emissions is significantly underestimated from WCS data. It is worth noting, though, that this factor only affects 25-33% of diurnal emissions. As the true diurnal cycle cannot be derived from WCS data, field data of repeat transects spanning the different phases of a diurnal cycle are needed.

4.7 Future needs and improvements

The sensitivity studies identified areas for improvement and data gaps. These are described in brief below and in more detail in **Supp. Sec. S8**. The largest uncertainty was with regards to partitioning between the inshore and offshore seep trends, which could be determined by a second air quality station, preferably including speciation such as by CEAS analyzers of CH_4, C_2H_6, and C_3H_8. Further simulations could add grid cells for evasion corresponding to the downcurrent plumes to assess their contribution. The model was limited by available workstation power; however, additional computation power could open improvements such as simulating a range of wind speeds based on the wind speed probability distribution with respect to wind direction, $\phi(u, \theta)$, e.g., Fig. 5.

Additional field work and data also are needed. Another important sensitivity was to boundary layer height, BL, which varies diurnally and seasonally (Dorman & Winant, 2000) and could be derived from ceilometer data (Münkel, 2007). Another significant concern is afternoon seep field emissions that bypass WCS, which could be addressed by field work and a second air quality station at a different downwind direction from the seep field. Mapping offshore wind fields to characterize wind veering across the seep field is needed to allow simulations to provide insights at the seep area size-scale.

Deleted: and

Deleted: .

Deleted: ,θ).

5 Conclusions

In this study, data from an onshore air quality station located downwind of a large marine seep field was analysed to derive the three-decade-averaged seep field emissions using an inversion model. The modeled emissions were similar to reported emissions; however, this was coincidental given that prior reported emissions were during a period of field quiescence. Highlighting the significance of the COP seep field, ethane and propane emissions suggest the COP seep field contributes 0.04% and 0.12% of the global seep budget, respectively. As a result, COP seep field emissions of 19 Gg CH_4 yr^{-1} are consistent with global geo-gas budgets of 45 Tg yr^{-1}, but inconsistent with significantly lower emissions estimated from ice core isotopic data. Additionally, the approach could be adapted to air quality station data for other sources including terrestrial seeps, production fields, etc., if the sources are spatially constrained and isolated from confounding sources.

Deleted: Tg

Data availability. All data needed to evaluate the conclusions in the paper are present in the paper and/or the Supplementary Materials and/or were submitted to the Mendeley Data Repository, see Leifer, Ira (2020), "Seep_Air_Data", Mendeley Data, V1, http://dx.doi.org/10.17632/znzhxkftm8.1

Supplement. The supplement contains additional supporting figures and details to complement the manuscript and an interactive map file as a Google Earth archive of the offshore survey data that are presented in **Fig. 2**.

Author Contributions. IL Developed and conducted the study, analysed data, and wrote the manuscript. CM analysed data and edited the manuscript. DB analysed air sample data and edited the manuscript.

Competing interests. The authors declare that they have no conflict of interest.

Acknowledgements. We would like to gratefully acknowledge the SBCAPCD for providing data from their ongoing monitoring program and the contribution of Marc Moritsch and Joel S. Cordes in particular for help with these data, and Doug Wilson for the processed sonar data. We recognize the skill and participation of vessel captains Jeff Wright and Tony Vultaggio and editorial review by Charlotte Marston, Bubbleology Research International.

Financial Support. This work was supported by Plains All American Pipeline and the Bubbleology Research International, Internal Research and Development (IRAD) fund.

References

Abrams, M. A. (2005). Significance of hydrocarbon seepage relative to petroleum generation and entrapment. *Marine and Petroleum Geology, 22*(4), 457-477. doi:10.1016/j.marpetgeo.2004.08.003

Abrams, M. A. (2017). Evaluation of near-surface gases in marine sediments to assess subsurface petroleum gas generation and entrapment. *Geosciences, 7*(2), 35. doi:10.3390/geosciences7020035

Bernard, B. B., Brooks, J. M., & Zumberge, J. (2001, 16-19 September 2001). *Determining the origin of gases in near-surface sediments.* Paper presented at the AAPG Hedberg Conference, Vancouver BC, Canada.

Boles, J. R., Clark, J. F., Leifer, I., & Washburn, L. (2001). Temporal variation in natural methane seep rate due to tides, Coal Oil Point area, California. *Journal Geophysical Research - Oceans, 106*(C11), 27,077-027,086. doi:10.1029/2000JC000774

Borges, A. V., Champenois, W., Gypens, N., Delille, B., & Harlay, J. (2016). Massive marine methane emissions from near-shore shallow coastal areas. *Scientific Reports, 6*, 27908. doi:10.1038/srep27908

Bradley, E. S., Leifer, I., & Roberts, D. A. (2010). Long-term monitoring of a marine geologic hydrocarbon source by a coastal air pollution station in Southern California. *Atmospheric Environment, 44*(38), 4973-4981. doi:10.1016/j.atmosenv.2010.08.010

CDOGGR. (2018). Well Finder. Retrieved from https://www.conservation.ca.gov/dog/Pages/Wellfinder.aspx. Retrieved 6 May 2019, from California Department of Conservation https://www.conservation.ca.gov/dog/Pages/Wellfinder.aspx

Ciotoli, G., Procesi, M., Etiope, G., Fracassi, U., & Ventura, G. (2020). Influence of tectonics on global scale distribution of geological methane emissions. *Nature Communications, 11*(1), 2305. doi:10.1038/s41467-020-16229-1

Clark, J. F., Washburn, L., Hornafius, J. S., & Luyendyk, B. P. (2000). Natural marine hydrocarbon seep source of dissolved methane to California coastal waters. *Journal Geophysical Research - Oceans, 105*, 11,509-511,522. doi:10.1029/2000JC000259

Clark, J. F., Washburn, L., & Schwager, K. (2010). Variability of gas composition and flux intensity in natural marine hydrocarbon seeps. *Geo-Marine Letters, 30*, 379-388. doi:10.1007/s00367-009-0167-1

Di, P., Feng, D., & Chen, D. (2019). The distribution of dissolved methane and its air-sea flux in the plume of a seep field, Lingtou Promontory, South China Sea. *Geofluids, 2019*, 3240697. doi:10.1155/2019/3240697

Di, P., Feng, D., Tao, J., & Chen, D. (2020). Using time-series videos to quantify methane bubbles flux from natural cold seeps in the South China Sea. *Minerals, 10*(3), 216. doi:10.3390/min10030216

Dorman, C. E., & Winant, C. D. (2000). The structure and variability of the marine atmosphere around the Santa Barbara Channel. *Monthly Weather Review, 128*(2), 261-282. doi:10.1175/1520-0493(2000)128<0261

Edinger, J. G. (1959). Changes in the depth of the marine layer over the Los Angeles Basin. *Journal of Meteorology, 16*(3), 219-226. doi:10.1175/1520-0469(1959)016<0219:citdot>2.0.co;2

Etiope, G., & Ciccioli, P. (2009). Earth's degassing: A missing ethane and propane source. *Science, 323*(5913), 478-478. doi:10.1126/science.1165904

1043 Etiope, G., Ciotoli, G., Schwietzke, S., & Schoell, M. (2019). Gridded maps of geological
1044 methane emissions and their isotopic signature. *Earth System Science Data, 11*(1), 1-22.
1045 doi:10.5194/essd-11-1-2019
1046 Etiope, G., & Schwietzke, S. (2019). Global geological methane emissions: An update of top-
1047 down and bottom-up estimates. *Elementa: Science of the Anthropocene, 7*.
1048 doi:10.1525/elementa.383
1049 Fischer, P. J. (1978). Oil and Tar Seeps, Santa Barbara Basin, California. In D. J. Everitts, R. G.
1050 Paul, C. F. Eaton, & E. E. Welday (Eds.), *California Offshore Gas, Oil and Tar Seeps*
1051 (pp. 1-62). Sacramento, California: California State Lands Commission.
1052 Freeworldmaps (Cartographer). (2020). Physical Map of California. Retrieved from
1053 https://www.freeworldmaps.net/united-states/california/map.html
1054 Frew, N. M., Bock, E. J., Schimpf, U., Hara, T., Haußecker, H., Edson, J. B., . . . Jähne, B.
1055 (2004). Air-sea gas transfer: Its dependence on wind stress, small-scale roughness, and
1056 surface films. *Journal of Geophysical Research: Oceans, 109*(C8), C08S17.
1057 doi:10.1029/2003JC002131
1058 Greinert, J. (2008). Monitoring temporal variability of bubble release at seeps: The
1059 hydroacoustic swath system GasQuant. *Journal of Geophysical Research, 113*, C07048.
1060 doi:10.1029/2007JC004704
1061 Greinert, J., McGinnis, D. F., Naudts, L., Linke, P., & De Batist, M. (2010). Atmospheric
1062 methane flux from bubbling seeps: Spatially extrapolated quantification from a Black Sea
1063 shelf area. *Journal of Geophysical Research, 115*. doi:10.1029/2009jc005381
1064 Hanna, S. R., Briggs, G. A., & Hosker Jr., R. P. (1982). *Handbook on Atmospheric Diffusion* (J.
1065 S. Smith Ed.): Technical Information Center, U.S. Department of Energy.
1066 Helmig, D., Rossabi, S., Hueber, J., Tans, P., Montzka, S. A., Masarie, K., . . . Pozzer, A. (2016).
1067 Reversal of global atmospheric ethane and propane trends largely due to US oil and
1068 natural gas production. *Nature Geoscience, 9*(7), 490-495. doi:10.1038/ngeo2721
1069 Heyer, J., & Berger, U. (2000). Methane emission from the coastal area in the Southern Baltic
1070 Sea. *Estuarine, Coastal and Shelf Science, 51*(1), 13-30. doi:10.1006/ecss.2000.0616
1071 Higgs, B., Mountjoy, J. J., Crutchley, G. J., Townend, J., Ladroit, Y., Greinert, J., & McGovern,
1072 C. (2019). Seep-bubble characteristics and gas flow rates from a shallow-water, high-
1073 density seep field on the shelf-to-slope transition of the Hikurangi subduction margin.
1074 *Marine Geology, 417*, 105985. doi:10.1016/j.margeo.2019.105985
1075 Hmiel, B., Petrenko, V. V., Dyonisius, M. N., Buizert, C., Smith, A. M., Place, P. F., . . .
1076 Dlugokencky, E. (2020). Preindustrial 14CH4 indicates greater anthropogenic fossil CH4
1077 emissions. *Nature, 578*(7795), 409-412. doi:10.1038/s41586-020-1991-8
1078 Höglund-Isaksson, L. (2017). Bottom-up simulations of methane and ethane emissions from
1079 global oil and gas systems 1980 to 2012. *Environmental Research Letters, 12*(2), 024007.
1080 doi:10.1088/1748-9326/aa583e
1081 Hornafius, S. J., Quigley, D. C., & Luyendyk, B. P. (1999). The world's most spectacular marine
1082 hydrocarbons seeps (Coal Oil Point, Santa Barbara Channel, California): Quantification
1083 of emissions. *Journal Geophysical Research - Oceans, 104*(C9), 20,703-720,711.
1084 doi:10.1029/1999JC900148
1085 Hughes, M., Hall, A., & Fovell, R. G. (2007). Dynamical controls on the diurnal cycle of
1086 temperature in complex topography. *Climate Dynamics, 29*(2), 277-292.
1087 doi:10.1007/s00382-007-0239-8

IEA. (2020). *Methane Tracker 2020*. Retrieved from Paris: https://www.iea.org/reports/methane-tracker-2020

IPCC. (2013). *Working Group 1 Contribution to the IPCC Fifth Assessment Report Climate Change 2013-The Physical Science Basis*. Retrieved from IPCC Secretariat, Geneva, Switzerland:

IPCC. (2014). *Climate Change 2014: Synthesis Report. Contributions of Working Groups I, II and III to the Fifth Assessment Report of the Intergovernmental Panel on Climate Change*. Retrieved from Geneva, Switzerland: http://www.ipcc.ch/pdf/assessment-report/ar5/syr/SYR_AR5_FINAL_full_wcover.pdf

Jackson, R. B., Saunois, M., Bousquet, P., Canadell, J. G., Poulter, B., Stavert, A. R., . . . Tsuruta, A. (2020). Increasing anthropogenic methane emissions arise equally from agricultural and fossil fuel sources. *Environmental Research Letters, 15*(7), 071002. doi:10.1088/1748-9326/ab9ed2

Johansen, C., Macelloni, L., Natter, M., Silva, M., Woosley, M., Woolsey, A., . . . MacDonald, I. R. (2020). Hydrocarbon migration pathway and methane budget for a Gulf of Mexico natural seep site: Green Canyon 600. *Earth and Planetary Science Letters, 545*, 116411. doi:10.1016/j.epsl.2020.116411

Johansen, C., Todd, A. C., & MacDonald, I. R. (2017). Time series video analysis of bubble release processes at natural hydrocarbon seeps in the Northern Gulf of Mexico. *Marine and Petroleum Geology, 82*, 21-34. doi:https://doi.org/10.1016/j.marpetgeo.2017.01.014

Jordan, S. F. A., Treude, T., Leifer, I., Janßen, R., Werner, J., Schulz-Vogt, H., & Schmale, O. (2020). Bubble-mediated transport of benthic microorganisms into the water column: Identification of methanotrophs and implication of seepage intensity on transport efficiency. *Scientific Reports, 10*(1), 4682. doi:10.1038/s41598-020-61446-9

Judd, A., & Hovland, M. (2007). *Seabed fluid flow: The impact on geology, biology and the marine environment*. Cambridge, UK: Cambridge University Press.

Kasaya, T., Mitsuzawa, K., Goto, T.-n., Iwase, R., Sayanagi, K., Araki, E., . . . Nagao, T. (2009). Trial of multidisciplinary observation at an expandable sub-marine cabled station "Off-Hatsushima Island Observatory" in Sagami Bay, Japan. *Sensors, 9*(11), 9241-9254. doi:10.3390/s91109241

Leifer, I. (2010). Characteristics and scaling of bubble plumes from marine hydrocarbon seepage in the Coal Oil Point seep field. *Journal Geophysical Research, 115*(C11), C11014. doi:10.1029/2009JC005844

Leifer, I. (2015). Seabed bubble flux estimation by calibrated video survey for a large blowout seep in the North Sea. *Journal of Marine and Petroleum Geology, 68B*, 743-752. doi:10.1016/j.marpetgeo.2015.08.032

Leifer, I. (2019). A synthesis review of emissions and fates for the Coal Oil Point marine hydrocarbon seep field and California marine seepage. *Geofluids, 2019*(4724587), 1-48. doi:10.1155/2019/4724587

Leifer, I., & Boles, J. (2005). Turbine tent measurements of marine hydrocarbon seeps on subhourly timescales. *Journal of Geophysical Research-Oceans, 110*(C1), C01006. doi:10.1029/2003jc002207

Leifer, I., Boles, J. R., Luyendyk, B. P., & Clark, J. F. (2004). Transient discharges from marine hydrocarbon seeps: Spatial and temporal variability. *Environmental Geology, 46*(8), 1038-1052. doi:10.1007/s00254-004-1091-3

Leifer, I., Chernykh, D., Shakhova, N., & Semiletov, I. (2017). Sonar gas flux estimation by bubble insonification: Application to methane bubble flux from seep areas in the outer Laptev Sea. *The Cryosphere, 11*(3), 1333-1350. doi:10.5194/tc-11-1333-2017

Leifer, I., & Clark, J. F. (2002). Modeling trace gases in hydrocarbon seep bubbles: Application to marine hydrocarbon seeps in the Santa Barbara Channel. *Geologiya I Geofizika, 47*(7), 572-579.

Leifer, I., Clark, J. F., & Chen, R. F. (2000). Modifications of the local environment by natural marine hydrocarbon seeps. *Geophysical Research Letters, 27*(22), 3711-3714. doi:10.1029/2000GL011619

Leifer, I., Jeuthe, H., Gjøsund, S. H., & Johansen, V. (2009). Engineered and natural marine seep, bubble-driven buoyancy flows. *Journal of Physical Oceanography, 39*(12), 3071-3090. doi:10.1175/2009JPO4135.1

Leifer, I., Kamerling, M., Luyendyk, B. P., & Wilson, D. (2010). Geologic control of natural marine hydrocarbon seep emissions, Coal Oil Point seep field, California. *Geo-Marine Letters, 30*(3-4), 331-338. doi:10.1007/s00367-010-0188-9

Leifer, I., Luyendyk, B. P., Boles, J., & Clark, J. F. (2006). Natural marine seepage blowout: Contribution to atmospheric methane. *Global Biogeochemical Cycles, 20*(3), GB3008. doi:10.1029/2005GB002668

Leifer, I., & MacDonald, I. (2003). Dynamics of the gas flux from shallow gas hydrate deposits: interaction between oily hydrate bubbles and the oceanic environment. *Earth and Planetary Science Letters, 210*(3-4), 411-424. doi:10.1016/S0012-821X(03)00173-0

Leifer, I., Melton, C., Fischer, M. L., Fladeland, M., Frash, J., Gore, W., . . . Yates, E. L. (2018). Atmospheric characterization through fused mobile airborne and surface in situ surveys: Methane emissions quantification from a producing oil field. *Atmospheric Measurement Techniques, 11*(3), 1689-1705. doi:10.5194/amt-11-1689-2018

Leifer, I., Melton, C., Manish, G., & Leen, B. (2014). Mobile monitoring of methane leakage. *Gases and Instrumentation, July/August 2014*, 20-24.

Leifer, I., Melton, C., Tratt, D. M., Buckland, K. N., Chang, C., Frash, J., . . . Yurganov, L. (2018). Validation of mobile in situ measurements of dairy husbandry emissions by fusion of airborne/surface remote sensing with seasonal context from the Chino Dairy Complex. *Environmental Pollution, 242*(Pt B), 2111-2134. doi:10.1016/j.envpol.2018.03.078

Leifer, I., Melton, C., Tratt, D. M., Buckland, K. N., Clarisse, L., Coheur, P., . . . Yurganov, L. (2016). Remote sensing and in situ measurements of methane and ammonia emissions from a megacity dairy complex: Chino, CA. *Environmental Pollution, 221*, 37-51. doi:10.1016/j.envpol.2016.09.083

Leifer, I., & Patro, R. (2002). The bubble mechanism for methane transport from the shallow seabed to the surface: A review and sensitivity study. *Continental Shelf Research, 22*(16), 2409-2428. doi:10.1016/S0278-4343(02)00065-1

Leifer, I., Solomon, E., Schneider v. Deimling, J., Coffin, R., Rehder, G., & Linke, P. (2015). The fate of bubbles in a large, intense bubble plume for stratified and unstratified water: Numerical simulations of 22/4b expedition field data. *Journal of Marine and Petroleum Geology, 68B*, 806-823. doi:10.1016/j.marpetgeo.2015.07.025

Liss, P. S., & Duce, R. A. (2005). *The sea surface and global change*: Cambridge University Press.

Liss, P. S., & Merlivat, L. (1986). Air-sea gas exchange rates: Introduction and synthesis. In P. Buat-Ménard (Ed.), *THe Role of Air-Sea Exchange in Geochemical Cycling* (Vol. 185). Dordrecht: Springer.

Lu, R., Turco, R. P., & Jacobson, M. Z. (1997). An integrated air pollution modeling system for urban and regional scales: 1. Structure and performance. *Journal of Geophysical Research: Atmospheres, 102*(D5), 6063-6079. doi:10.1029/96jd03501

Marinaro, G., Etiope, G., Bue, N. L., Favali, P., Papatheodorou, G., Christodoulou, D., . . . Rolin, J.-F. (2006). Monitoring of a methane-seeping pockmark by cabled benthic observatory (Patras Gulf, Greece). *Geo-Marine Letters, 26*(5), 297-302. doi:10.1007/s00367-006-0040-4

Mazzini, A., Sciarra, A., Etiope, G., Sadavarte, P., Houweling, S., Pandey, S., & Husein, A. (2021). Relevant methane emission to the atmosphere from a geological gas manifestation. *Scientific Reports, 11*(1), 4138. doi:10.1038/s41598-021-83369-9

Minor, S. A., Kellogg, K. S., Stanley, R. G., Gurrola, L. D., Keller, E. A., & Brandt, T. R. (Cartographer). (2009). Geologic Map of the Santa Barbara Coastal Plain Area, Santa Barbara County, California. Retrieved from https://pubs.usgs.gov/sim/3001/

Münkel, C. (2007). Mixing height determination with lidar ceilometers - Results from Helsinki Testbed. *Meteorologische Zeitschrift, 16*, 451-459. doi:10.1127/0941-2948/2007/0221

Muyakshin, S. I., & Sauter, E. (2010). The hydroacoustic method for the quantification of the gas flux from a submersed bubble plume. *Oceanology, 50*(6), 995-1001. doi:10.1134/S0001437010060202

Nicewonger, M. R., Verhulst, K. R., Aydin, M., & Saltzman, E. S. (2016). Preindustrial atmospheric ethane levels inferred from polar ice cores: A constraint on the geologic sources of atmospheric ethane and methane. *Geophysical Research Letters, 43*(1), 214-221. doi:https://doi.org/10.1002/2015GL066854

Nightingale, P. D., Malin, G., Law, C. S., Watson, A. J., Liss, P. S., Liddicoat, M. I., . . . Upstill-Goddard, R. C. (2000). In situ evaluation of air-sea gas exchange parameterizations using novel conservative and volatile tracers. *Global Biogeochemical Cycles, 14*(1), 373-387. doi:10.1029/1999GB900091

Nisbet, E. G., Manning, M. R., Dlugokencky, E. J., Fisher, R. E., Lowry, D., Michel, S. E., . . . White, J. W. C. (2019). Very strong atmospheric methane growth in the 4 years 2014–2017: Implications for the Paris Agreement. *Global Biogeochemical Cycles, 33*(3), 318-342. doi:10.1029/2018GB006009

Olson, D. J. (1983). *Surface and subsurface geology of the Santa Barbara Goleta Metropolitan area, Santa Barbara County, California.* (MS). Oregon State University, Retrieved from https://ir.library.oregonstate.edu/concern/graduate_thesis_or_dissertations/v692tb957?locale=it

Padilla, A. M., Loranger, S., Kinnaman, F. S., Valentine, D. L., & Weber, T. C. (2019). Modern assessment of natural hydrocarbon gas flux at the Coal Oil Point seep field, Santa Barbara, California. *Journal of Geophysical Research: Oceans, 124*(4), 2472-2484. doi:10.1029/2018jc014573

Peischl, J., Ryerson, T. B., Brioude, J., Aikin, K. C., Andrews, A. E., Atlas, E., . . . Parrish, D. D. (2013). Quantifying sources of methane using light alkanes in the Los Angeles basin, California. *Journal of Geophysical Research: Atmospheres, 118*(10), 4974-4990. doi:10.1002/jgrd.50413

Pozzer, A., Pollmann, J., Taraborrelli, D., Jöckel, P., Helmig, D., Tans, P., . . . Lelieveld, J. (2010). Observed and simulated global distribution and budget of atmospheric C₂-C₅ alkanes. *Atmospheric Chemistray and Physics, 10*(9), 4403-4422. doi:10.5194/acp-10-4403-2010

Rahn, D. A., Parish, T. R., & Leon, D. (2017). Synthesis of observations from the Precision Atmospheric Marine Boundary Layer Experiment (PreAMBLE). *Monthly Weather Review, 145*(6), 2325-2342. doi:10.1175/mwr-d-16-0373.1

Reeburgh, W. S. (2007). Oceanic methane biogeochemistry. *Chemical Reviews, 107*(2), 486-513. doi:10.1021/cr050362v

Reeburgh, W. S., Ward, B. B., Whalen, S. C., Sandbeck, K. A., Kilpatrickt, K. A., & Kerkhof, L. J. (1991). Black Sea methane geochemistry. *Deep Sea Research Part A. Oceanographic Research Papers, 38*, S1189-S1210. doi:https://doi.org/10.1016/S0198-0149(10)80030-5

Rehder, G., Keir, R. S., Suess, E., & Rhein, M. (1999). Methane in the Northern Atlantic controlled by microbial oxidation and atmospheric history. *Geophysical Research Letters, 26*(5), 587-590. doi:10.1029/1999GL900049

Riedel, M., Scherwath, M., Römer, M., Veloso, M., Heesemann, M., & Spence, G. D. (2018). Distributed natural gas venting offshore along the Cascadia margin. *Nature Communications, 9*(1), 3264. doi:10.1038/s41467-018-05736-x

Römer, M., Hsu, C.-W., Loher, M., MacDonald, I. R., dos Santos Ferreira, C., Pape, T., . . . Sahling, H. (2019). Amount and fate of gas and oil discharged at 3400 m water depth from a natural seep site in the Southern Gulf of Mexico. *Frontiers in Marine Science, 6*(700). doi:10.3389/fmars.2019.00700

Römer, M., Riedel, M., Scherwath, M., Heesemann, M., & Spence, G. D. (2016). Tidally controlled gas bubble emissions: A comprehensive study using long-term monitoring data from the NEPTUNE cabled observatory offshore Vancouver Island. *Geochemistry, Geophysics, Geosystems, 17*(9), 3797-3814. doi:10.1002/2016GC006528

Römer, M., Sahling, H., Pape, T., Bohrmann, G., & Spieß, V. (2012). Quantification of gas bubble emissions from submarine hydrocarbon seeps at the Makran continental margin (offshore Pakistan). *Journal of Geophysical Research: Oceans, 117*(C10), C10015. doi:10.1029/2011jc007424

Römer, M., Wenau, S., Mau, S., Veloso, M., Greinert, J., Schlüter, M., & Bohrmann, G. (2017). Assessing marine gas emission activity and contribution to the atmospheric methane inventory: A multidisciplinary approach from the Dutch Dogger Bank seep area (North Sea). *Geochemistry, Geophysics, Geosystems, 18*(7), 2617-2633. doi:10.1002/2017gc006995

Saunois, M., Stavert, A. R., Poulter, B., Bousquet, P., Canadell, J. G., Jackson, R. B., . . . Zhuang, Q. (2020). The global methane budget 2000-2017. *Earth System Science Data, 12*(3), 1561-1623. doi:10.5194/essd-2019-128

Sauter, E. J., Muyakshin, S. I., Charlou, J.-L., Schlüter, M., Boetius, A., Jerosch, K., . . . Klages, M. (2006). Methane discharge from a deep-sea submarine mud volcano into the upper water column by gas hydrate-coated methane bubbles. *Earth and Planetary Science Letters, 243*(3-4), 354-365. doi:10.1016/j.epsl.2006.01.041

Scherwath, M., Thomsen, L., Riedel, M., Römer, M., Chatzievangelou, D., Schwendner, J., . . . Heesemann, M. (2019). Ocean observatories as a tool to advance gas hydrate research. *Earth and Space Science, 6*(12), 2644-2652. doi:10.1029/2019ea000762

Schmale, O., Beaubien, S. E., Rehder, G., Greinert, J., & Lonmbardi, S. (2010). Gas seepage in the Dnepr paleo-delta area (NW-Black Sea) and its regional impact on the water column methane cycle. *Journal of Marine Systems, 80*(1-2), 90-100. doi:10.1016/j.jmarsys.2009.10.003

Schmale, O., Greinert, J., & Rehder, G. (2005). Methane emission from high-intensity marine gas seeps in the Black Sea into the atmosphere. *Geophysical Research Letters, 32*(7), L07609. doi:10.1029/2004gl021138

Schmale, O., Leifer, I., Stolle, C., Schneider von Deimling, J., Krause, S., Kießlich, K., . . . Treude, T. (2015). Bubble transport mechanism: Indications for a gas bubble-mediated innoculation of benthic methanotrophs into the water column. *Continental Shelf Research, 103*, 70-78. doi:10.1016/j.csr.2015.04.022

Schneider von Deimling, J., Rehder, G., Greinert, J., McGinnis, D. F., Boetius, A., & Linke, P. (2011). Quantification of seep-related methane gas emissions at Tommeliten, North Sea. *Continental Shelf Research, 31*, 867-878. doi:10.1016/j.csr.2011.02.012

Schwietzke, S., Sherwood, O. A., Bruhwiler, L. M. P., Miller, J. B., Etiope, G., Dlugokencky, E. J., . . . Tans, P. P. (2016). Upward revision of global fossil fuel methane emissions based on isotope database. *Nature, 538*(7623), 88-91. doi:10.1038/nature19797

Shakhova, N., Semiletov, I., Leifer, I., Rekant, P., Salyuk, A., & Kosmach, D. (2010). Geochemical and geophysical evidence of methane release over the East Siberian Arctic Shelf. *Journal of Geophysical Research, 115*(C8), C08007. doi:10.1029/2009JC005602

Shakhova, N., Semiletov, I., Salyuk, A., Iossoupov, V., Kosmach, D., & Gustafsson, O. (2010). Extensive methane venting to the atmosphere from sediments of the East Siberian Arctic Shelf. *Science, 327*, 1246-1249. doi:10.1126/science.1182221

Shakhova, N., Semiletov Igor P., Leifer, I., Sergienko, V., Salyuk, A., Kosmach, D., . . . Gustafsson, O. (2013). Ebullition and storm-induced methane release from the East Siberian Arctic Shelf. *Nature Geoscience, 7*, 64-70. doi:10.1038/ngeo2007

Shindell, D. T., Faluvegi, G., Bell, N., & Schmidt, G. A. (2005). An emissions-based view of climate forcing by methane and tropospheric ozone. *Geophysical Research Letters, 32*, L04803. doi:doi:10.1029/2004GL021900

Simpson, I. J., Sulbaek Andersen, M. P., Meinardi, S., Bruhwiler, L., Blake, N. J., Helmig, D., . . . Blake, D. R. (2012). Long-term decline of global atmospheric ethane concentrations and implications for methane. *Nature, 488*(7412), 490-494. doi:10.1038/nature11342

Solomon, E., Kastner, M., MacDonald, I. R., & Leifer, I. (2009). Considerable methane fluxes to the atmosphere from hydrocarbon seeps in the Gulf of Mexico. *Nature Geoscience, 2*, 561-565. doi:10.1038/NGEO574

Thompson, D., Leifer, I., Bovensman, H., Eastwood, M., Fladeland, M., Frankenberg, C., . . . Thorpe, A. K. (2015). Real-time remote detection and measurement for airborne imaging spectroscopy: A case study with methane. *Atmospheric Measurement Techniques, 8*, 1-46. doi:10.5194/amtd-8-1-2015

Thornton, B. F., Prytherch, J., Andersson, K., Brooks, I. M., Salisbury, D., Tjernström, M., & Crill, P. M. (2020). Shipborne eddy covariance observations of methane fluxes constrain Arctic sea emissions. *Science Advances, 6*(5), eaay7934. doi:10.1126/sciadv.aay7934

Veloso-Alarcón, M. E., Jansson, P., De Batist, M., Minshull, T. A., Westbrook, G. K., Pälike, H., . . . Greinert, J. (2019). Variability of acoustically evidenced methane bubble emissions offshore Western Svalbard. *Geophysical Research Letters, 46*(15), 9072-9081. doi:10.1029/2019gl082750

Wanninkhof, R., Asher, W. E., Ho, D. T., Sweeney, C., & McGillis, W. R. (2009). Advances in quantifying air-sea gas exchange and environmental forcing. *Annual Review of Marine Science, 1*(1), 213-244. doi:10.1146/annurev.marine.010908.163742

Washburn, L., Johnson, C., Gotschalk, C. G., & Egland, E. T. (2001). A gas capture buoy for measuring bubbling gas flux in oceans and lakes. *Journal of Atmospheric and Oceanic Technology, 18*, 1411-1420. doi:10.1175/1520-0426

Weber, D., Marquez, B. A., Taylor, C., Raya, P., Contreras, P., Howard, D., . . . Doezema, L. A. (2017). Macroseepage of methane and light alkanes at the La Brea tar pits in Los Angeles. *Journal of Atmospheric Chemistry, 74*(3), 339-356. doi:10.1007/s10874-016-9346-4

Weber, T. C., Mayer, L., Jerram, K., Beaudoin, J., Rzhanov, Y., & Lovalvo, D. (2014). Acoustic estimates of methane gas flux from the seabed in a 6000 km2 region in the Northern Gulf of Mexico. *Geochemistry, Geophysics, Geosystems, 15*(5), 1911-1925. doi:10.1002/2014gc005271

Wiggins, S. M., Leifer, I., Linke, P., & Hildebrand, J. A. (2015). Long-term acoustic monitoring at North Sea well site 22/4b. *Journal of Marine and Petroleum Geology, 68*, 776-788. doi:10.1016/j.marpetgeo.2015.02.011

Wilson, D., Leifer, I., & Maillard, E. (2015). Megaplume bubble process visualization by 3D multibeam sonar mapping. *Journal of Marine and Petroleum Geology, 68B*, 753-765. doi:10.1016/j.marpetgeo.2015.07.007

Zhao, D., Toba, Y., Suzuki, Y., & Komori, S. (2003). Effect of wind waves on air'sea gas exchange: Proposal of an overall CO2 transfer velocity formula as a function of breaking-wave parameter. *Tellus B: Chemical and Physical Meteorology, 55*(2), 478-487. doi:10.3402/tellusb.v55i2.16747

Zhao, Y., Saunois, M., Bousquet, P., Lin, X., Berchet, A., Hegglin, M. I., . . . Zheng, B. (2020). Influences of hydroxyl radicals (OH) on top-down estimates of the global and regional methane budgets. *Atmospheric Chemistry Physics, 20*(15), 9525-9546. doi:10.5194/acp-20-9525-2020

Table of Nomenclature

NMHC	Non Methane Hydro Carbons
O&G	Oil and Gas
TC	Total Carbon
THC	Total HydroCarbon
WCS	West Campus Station
$C_{ave}(\theta)$	Wind direction-resolved average concentration
C_{CH4}	Methane concentration
$C_{max}(\theta)$	Wind direction-resolved maximum concentration
$C_{med}(\theta)$	Wind direction-resolved median concentration
C'_{Obs}	WCS observed concentration
C_{seep}	Concentration in seep directions
C'_{Sim}	WCS simulated concentration
$u_{ave}(\theta)$	Wind direction-resolved average u
$u_{max}(\theta)$	Wind direction-resolved maximum u
$u_{med}(\theta)$	Wind direction-resolved median u
u_{seep}	Wind speed in seep directions
BL	Boundary layer height
C	Concentration
$C(t,\theta)$	Wind direction and time-resolved average concentration
C'	Plume (anomaly) concentration
C_1-C_6	Methane to hexane concentrations
E_A	Atmospheric emissions
E_B	Seabed (bottom) emissions
$E_{i,j}$	Grid cell i, j atmospheric emissions
E_W	Emissions to the water column in the near field
i	Grid cell easting index
j	Grid cell northing index
$K(r,\theta)$	Wind direction and distance-resolved correction function to emissions
$K(\theta)$	Wind direction varying, distance correction function to emissions
r	Distance from WCS to cell i, j
R	Residual in C' after Gaussian functional fit
R^2	Correlation coefficient
t	Time
u	Wind speed
$u(\theta)$	Wind direction-resolved wind speed
x,y	Cartesian coordinate system in wind reference frame
Y	Northing offset of WCS
$\delta\theta$	Model wind direction angular resolution
$\phi(u)$	Wind probability distribution
$\phi(\theta,C)$	Wind direction and concentration-resolved probability distribution
$\phi(\theta,u)$	Wind direction and wind speed-resolved probability distribution
$\phi(\omega)$	Sonar return probability distribution
$\phi_n(E_A)$	Normalized atmospheric emissions probability
$\phi_n(\omega)$	Normalized sonar return probability distribution
θ	Wind direction
ω	Sonar return
ψ	Wind veering
ζ	Relative inshore and offshore emissions

Table 1. Atmospheric plume composition and model atmospheric emissions.

Gas	*THC* Fraction (%)	*TC** Fraction (%)	Emissions (m^3 dy^{-1})	Emissions (Mg yr^{-1})
CH_4	88.5	72.8	73,900	19,300
C_2H_6	3.10	2.55	2,590	1270
C_3H_8	4.18	3.44	3,510	2520
C_4H_{10}	2.76	2.27	2,300	2180
C_5H_{12}	1.11	0.92	930	1090
C_6H_{14}	0.133	0.11	110	150
C_6H_6	$7.8x10^{-5}$	$6.4x10^{-5}$	7.1	8.3
C_7H_{16}	0.036	0.030	29.7	45.8
C_7H_8	$1.8x10^{-5}$	$1.5x10^{-5}$	1.8	2.3
NMHC**	11.5	9.48	9,640	7410
*THC****	85	82.3	83,400	26,600
CO_2		17.7	21,600	15200
CO		0.003	3780	2660

**TC* is total carbon and is *THC*+CO+CO_2

***NMHC* is non methane hydrocarbons and is C_2-C_7

****THC* is total hydrocarbon and is C_1-C_7

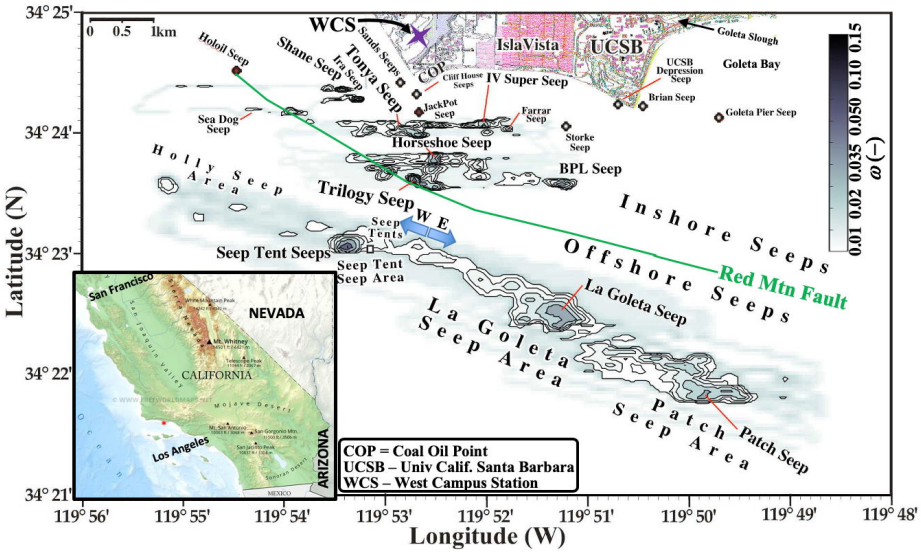

Figure 1: Sonar return, ω, map after Leifer et al. (2010). Purple star marks West Campus Station (WCS). Seep names are informal (Table S3), font size corresponds to strength. E-W arrow segregates east and west offshore seepage. Data keys on panels. Inset shows S. California, red dot marks COP seep field. California inset map from Freeworldmaps (2020).

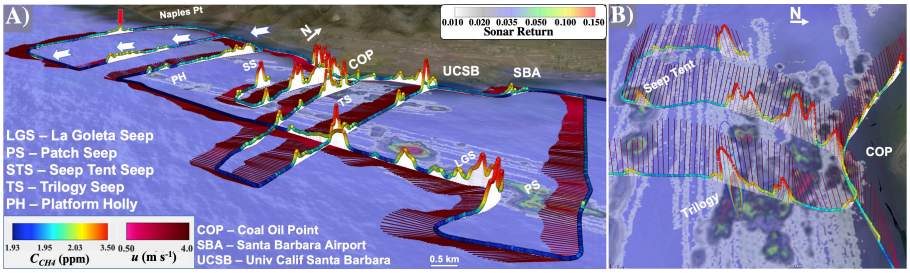

Figure 2: A) Methane, C_{CH4}, and wind, u, data for 28 May 2016. White arrows show canyon offshore flow. Red arrows show unmapped seepage to the west of the COP seep field. B) C_{CH4} and u showing Gaussian plume model for Trilogy Seep. Sonar return map shown on sea surface. Data key and seep name key on panel. Displayed in the © GoogleEarth environment. See Supp. Fig. S6 for overhead view.

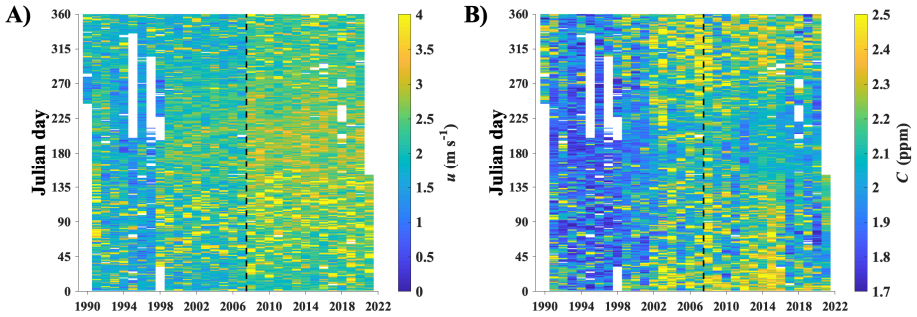

Figure 3: A) Daily mean wind speed, *u*, and B) concentration, *C*. Data key on figure. WCS upgrade on Jan 2008 is shown by a dashed black line. Supp. Fig. S7 shows raw dataset.

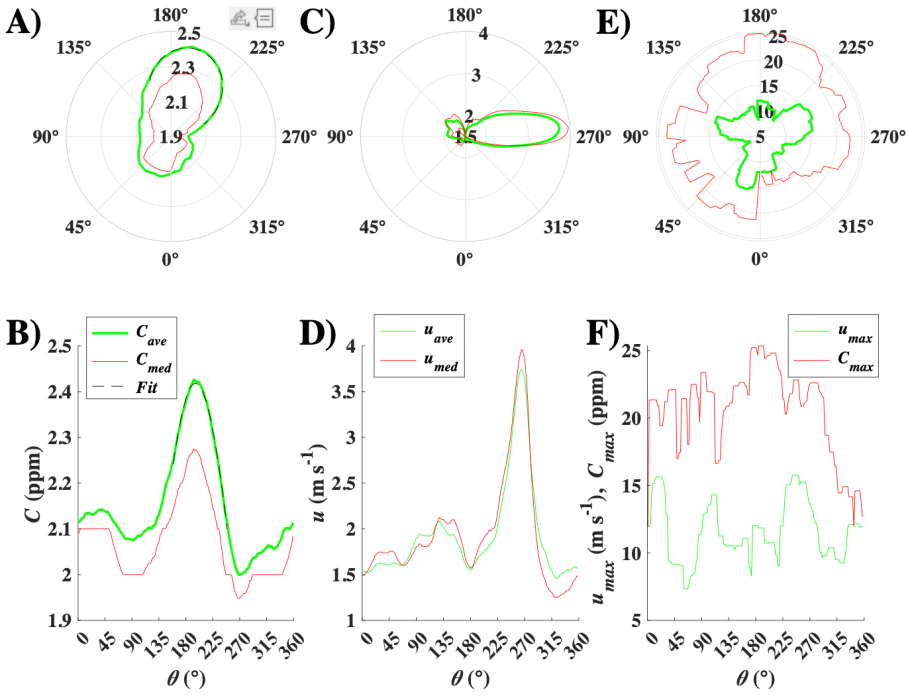

Figure 4: A, B) Concentration, C, versus wind-direction, θ, 1990-2021 for average, $\boldsymbol{C_{ave}(\theta)}$, and median, $\boldsymbol{C_{med}(\theta)}$, and fit to $\boldsymbol{C_{ave}(\theta)}$ for 155<θ<250°. Data key on panel B. C, D) Wind speed, u, average, $\boldsymbol{u_{ave}(\theta)}$, and median, $\boldsymbol{u_{med}(\theta)}$, Data key on panel D. and E, F) Maximum C, $\boldsymbol{C_{max}(\theta)}$, and wind speed, $\boldsymbol{u_{max}(\theta)}$. Data key on panel F. Polar plot oriented as at WCS facing the COP seep field.

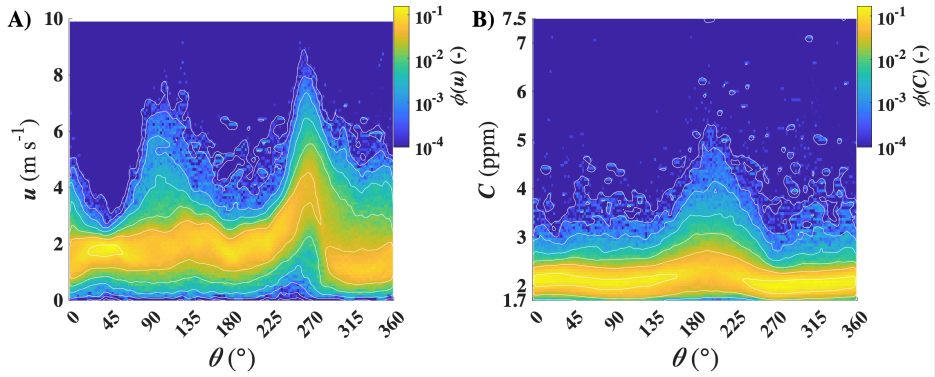

Figure 5: A) Wind-direction, θ, and wind-speed, u, resolved probability distribution, $\phi(\theta,\boldsymbol{u})$ and B) Concentration probability distribution, $\phi(\theta,C)$, for 1990-2016. White dashed line shows edges of seep field. Data key on figure.

Deleted: (

Deleted: θ)

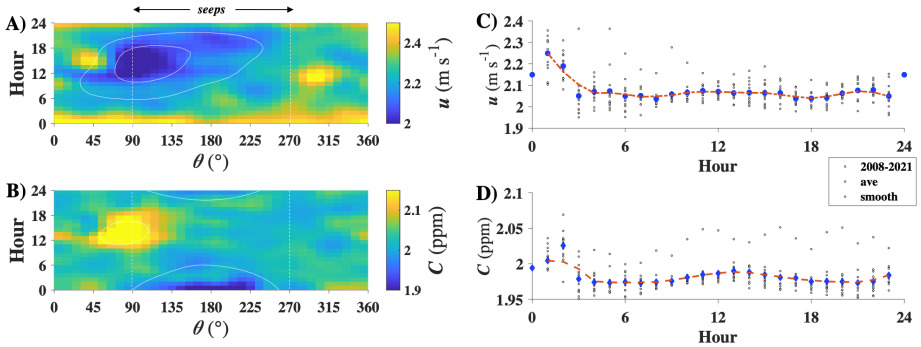

Figure 6: A) 2008-2021 hour- and wind direction-, θ, resolved wind speed, u, and B) concentration, C. C) Hourly-resolved, seep-direction (90–270°), wind speed, u, and D) concentration, C, averaged, individual years, and 3-year smoothed. Data key on figure. Midnight data missing due to daily calibration.

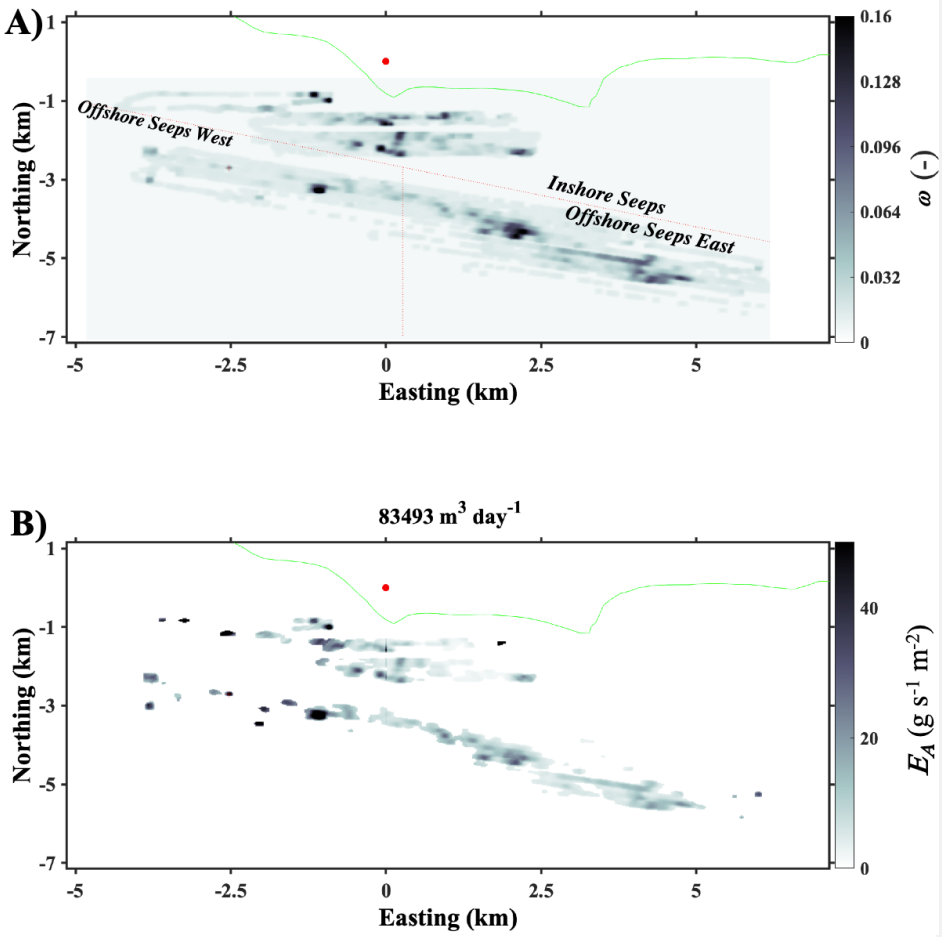

Figure 7: A) Sonar return, ω, gridded at 22-m resolution. B) Atmospheric emissions, E_A. West campus station (red dot) is at coordinate system origin. Green line is coast line.

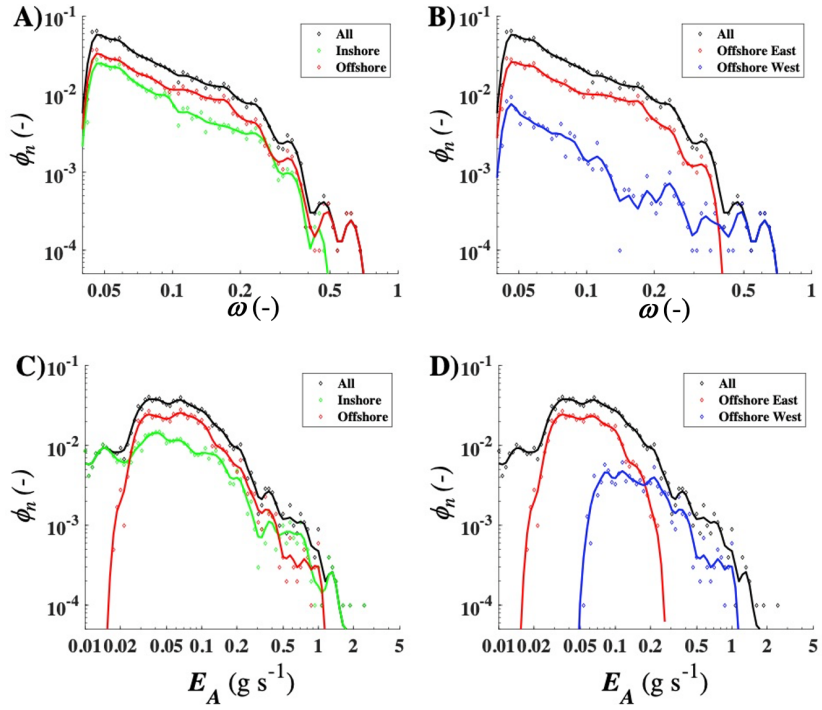

Figure 8: A) Sonar return, ω, occurrence probability, $\phi_n(\omega)$, for all seepage, inshore and offshore seepage and B) all seepage, offshore east seepage, and offshore west seepage. C) Atmospheric emission, E_A, occurrence probability, $\phi_n(E_A)$, for all seepage, inshore and offshore seepage and D) all seepage, offshore east seepage, and offshore west seepage. Data key on panels.

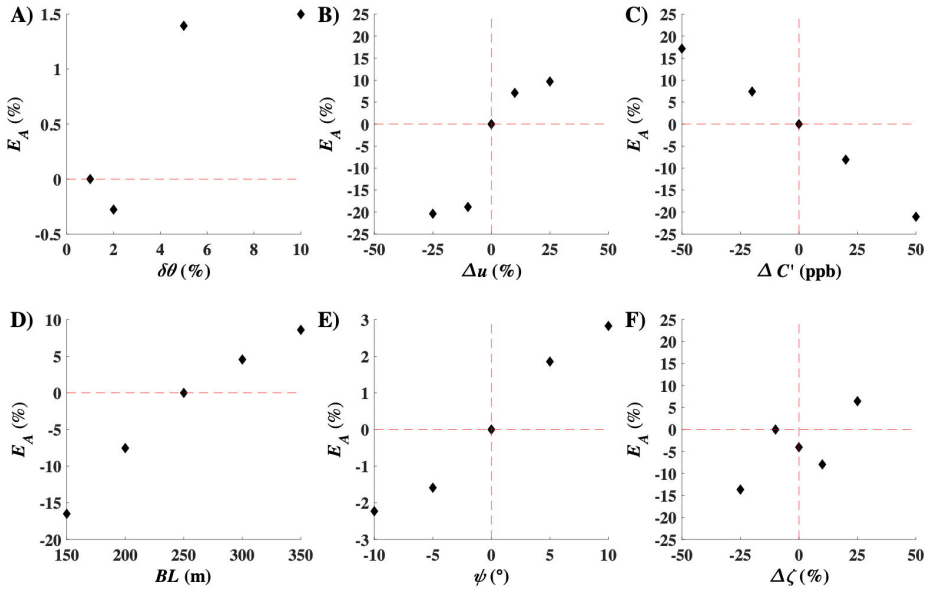

Figure 9: Emissions, E_A, sensitivity to uncertainty in A) model angular resolution, $\delta\theta$, B) wind speed variation, Δu, C) concentration anomaly variation, $\Delta C'$, D) boundary layer thickness, BL, E) wind veering, ψ, and F) inshore/offshore partition variation, $\Delta\zeta$. Note different units on different plots. See text for details.

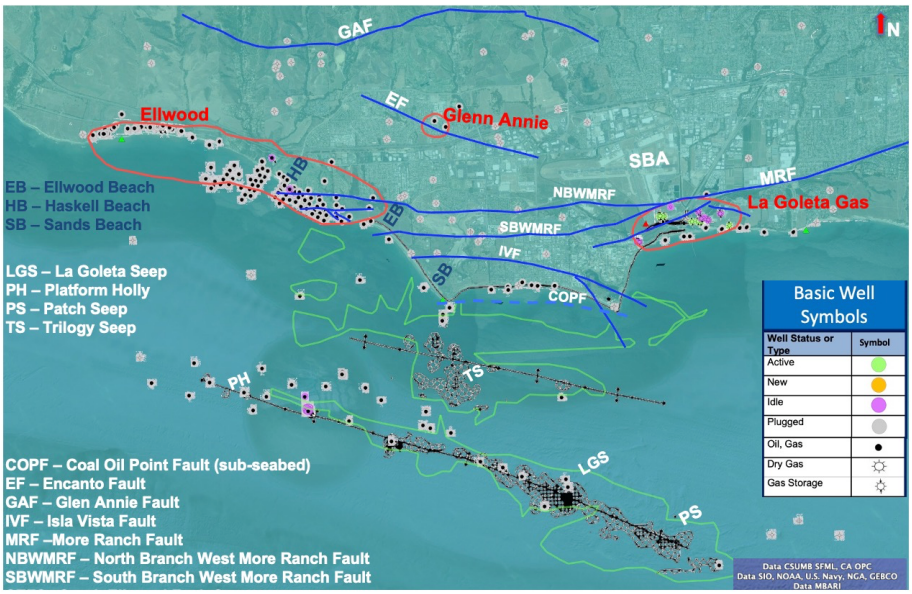

Figure 10: Map of the Goleta Plains oil and gas fields, wells, and the Coal Oil Point (COP) seep field. Grey hatch shows 1995 field extent, green outlines the 1940 field extent is from Leifer (2019). Field locations from Olson (1983). Well data from CDOGGR (2018). Faults from Minor et al. (2009). Seep names are informal. Data keys on panels. Shown in the © Google Earth environment.